

Article

Elemental Behavior during Weathering and Pedogenesis of Clay-Rich Red Soils Developed in Different Lithologies in Java–Madura and Sulawesi in Indonesia

Howard Omar Beckford ¹ , Cheng Chang ¹ and Hongbing Ji ^{1,2,*} 

¹ School of Energy and Environmental Engineering, University of Science and Technology Beijing, Beijing 100083, China

² State Key Laboratory of Environmental Geochemistry, Institute of Geochemistry, Chinese Academy of Sciences, Guiyang 550002, China

* Correspondence: ji.hongbing@hotmail.com; Tel.: +86-10-6233-2750; Fax: +86-10-6233-2750

Abstract: Clay-rich red soil profiles developed in different lithologies in Indonesia were assessed using geochemical evidence, the migration coefficient and elemental ratios. Our study aimed to ascertain the source of red soil materials and to investigate the elemental behavior in tropical soils. The results indicate carbonate profiles were derived from in situ weathering, while basalt profiles, even though having close affinity to their bedrock, also showed the contribution of external materials. Elemental behavior was dynamic with carbonate profiles indicating relatively constant depletion and even distribution. Basalt profiles indicated uneven distribution with enrichment and depletion. The variation in elemental behavior was linked to difference in lithologies, age and physiochemical conditions. Our findings support evidence of both residual and multiple source parent materials in red soil formation and provide insights into elemental behavior during weathering, while highlighting the influence of external materials' contribution in deeply weathered tropical soils.

Keywords: weathering; carbonate; basalt bedrock; lithology; Indonesia; tropical; red soils



Citation: Beckford, H.O.; Chang, C.; Ji, H. Elemental Behavior during Weathering and Pedogenesis of Clay-Rich Red Soils Developed in Different Lithologies in Java–Madura and Sulawesi in Indonesia. *Sustainability* **2023**, *15*, 4936. <https://doi.org/10.3390/su15064936>

Academic Editor: Guannan Liu

Received: 29 January 2023

Revised: 1 March 2023

Accepted: 6 March 2023

Published: 10 March 2023



Copyright: © 2023 by the authors. Licensee MDPI, Basel, Switzerland. This article is an open access article distributed under the terms and conditions of the Creative Commons Attribution (CC BY) license (<https://creativecommons.org/licenses/by/4.0/>).

1. Introduction

Red soils have distinct characteristics such as high iron oxide and clay contents and rubification, and are usually distributed in warm and humid areas around the Earth's surface [1–5]. Indonesia is the largest archipelago in the world that consists of clay-rich red soils distributed over high and low altitudinal range with a tropical monsoon climate. Generally, red soil is used to describe soils that have a hue value of 5 YR to 10 YR, and chroma ranging from 2 to 8 [6]. According to World Reference Base for Soil Resources [7] red soils are equivalent to Acrisols, Lixisols, Luvisols and Nitisols. There is still a long-standing debate as to the origin of red soils and their relation to the underlying bedrock. Researchers all over the world have put forward seven possible theories to explain the origin of red soils, including (1) detrital, (2) metasomatic, (3) residual and modified residual, (4) allochthonous, (5) eolian, (6) isovolumetric weathering and (7) poly-original theories [8]. Basically, the theories ascribe two main viewpoints, which differ by detrital and residual origin [9]. It is a commonly believed that chemical weathering predominantly contributes to the formation and evolution of red soils [10]. Chemical weathering of rocks is an important geochemical process that has contributed significantly to land morphology, chemical cycling, CO₂ consumption, terrestrial carbon cycle and climatic changes [11–20]. The nature and rate of chemical weathering vary widely and are influenced by many factors, such as lithology, topography, climate and biological activities [21]. Geochemical evidence has been long used to study the inheritance relationships between soils, weathering products and bedrocks [22–27]. However, not much comparative study has been done on the geochemical characteristics of different lithologies in relation to the overlying soil profile of

weathering products and weathering degree. Therefore, in the context of our paper, we used geochemical evidence from major elements, trace elements and rare earth elements (REEs). The paper aimed to ascertain the source of red soil materials and to investigate the elemental behavior and weathering degree across different lithologies in deeply weathered tropical soils.

2. Geography and Geological Setting

2.1. Materials and Methods

The territory of Indonesia stretches from $6^{\circ}08'$ north latitude to $11^{\circ}15'$ south latitude and from $94^{\circ}45'$ to $141^{\circ}05'$ east longitude (Figure 1). It is the largest archipelago in the world that consists of five major islands and approximately 30 smaller islands. The five main islands are Sumatra ($473,606 \text{ km}^2$), Java–Madura ($132,107 \text{ km}^2$), Kalimantan ($539,460 \text{ km}^2$), Sulawesi ($189,216 \text{ km}^2$) and Papua ($421,981 \text{ km}^2$). The average annual rainfall in Indonesia is approximately 2350 mm, with Java experiencing 2680 mm and Sulawesi 2340 mm/year [28]. The region experiences a west monsoon that brings rain from December to March and east monsoon that brings dry weather conditions from June to September. The annual temperature ranges from 21 to 33°C ; however, it is much lower at higher altitudes. The average humidity lies in the range 75–100%.

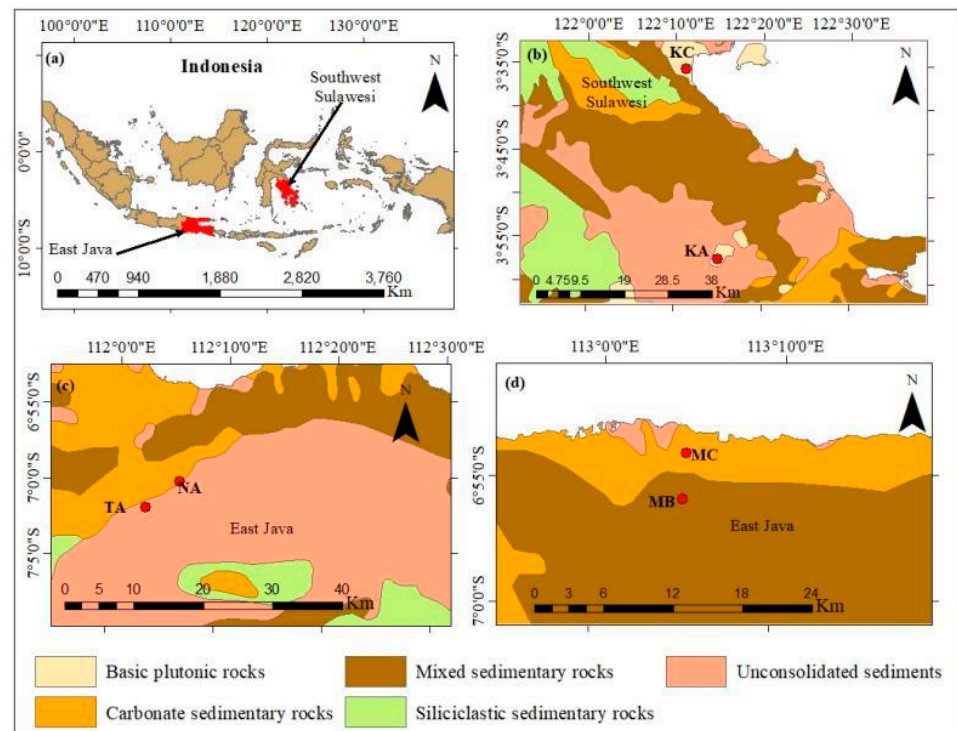


Figure 1. (a) Map showing location of study area of Java–Madura and Sulawesi in Indonesia and (b–d) illustrations of the locations of soil profiles within study area. The red dots represent the different soil sections included in the study.

Geologically, the archipelago islands are composed of continental blocks with both active and extinct volcanic arcs associated with subduction complexes of old and young oceanic basins. Java–Madura is one of the study areas that formed predominantly during the Tertiary and Quaternary period that is composed of mainly rhyolitic, dacitic–andesitic tuff, breccia and lava, partially intercalated with sandstone, shale, carbonaceous tuff and mudstone [29]. Sulawesi is the other study area that is dominated by an ultramafic complex. Strong tectonic activities in the area resulted in complex geological structures. Other lithological units, such as alluvial and sedimentary lacustrine rocks of Quaternary and Cretaceous sedimentary rocks, are present in and around the area [30].

2.2. Sampling and Analytical Methods

A total of six red soil profiles located 20–139 m above sea level from Java–Madura (carbonate) and Sulawesi (basalt) were selected. Fresh samples were collected according to stratigraphic order from representative horizons using the channeling sampling method. The location, elevation, thickness and visible characteristics of the soil profiles are illustrated in Table 1 and Figure 1. The profiles vary in depth, ranging from 85 to 210 cm and consist of 3–4 distinct horizons; namely, bedrock, saprock (fractured bedrock), regolith (subsoil) and upper soil surface layer (Figure 2). The surface soil layer of the carbonate profiles comprises loose soil covered by tropical rain (mixed) forests, with a few regenerated eucalyptus (*Eucalyptus urophylla*) and teak (*Tectona grandis*) trees. Directly below the soil surface layer, a red-brown and yellow-brown fine homogeneous laterite soil layer (regolith) was found, followed by a thin layer of grayish-white powdered layer (rock powder) in the MB and MC profiles. Below the powdered layer, saprock and/or bedrock layers can be found (Figure 2). The grayish-white powdered layer was absent from the basalt profiles (KA and KC); however, the KC profile contained a thin layer of purple ferruginous crust at the KC-4 position, intercepting the homogenous red regolith layer in the subsoil horizon. Similarly, the vegetation includes a mixed understory of tropical rain forest with families from Euphorbiaceae, Rubiaceae and Myrtaceae well represented in the area. A graphical representation of each profile is shown in Figure 2.

Table 1. The location, elevation, thickness and visible characteristics of six studied profiles in Indonesia.

| Soil Profiles | Location | Elevation (m) | Thickness (cm) | Parent Material | Soil Texture | Visible Characteristics |
|---------------|--------------------------|---------------|----------------|-----------------|-----------------|--|
| TA | 7°1'56" S, 112°3'6" E | 139 | 120 | Limestone | Silty clay loam | Gray soil layer with crushed stones Red with semi weathered bedrock layer |
| MB | 6°55'57" S, 113°4'46" E | 85.1 | 140 | Limestone | Silty loam | Red-brown |
| NA | 7°0'14" S, 112°6'5" E | 89 | 210 | Dolomite | Silty loam | Brown-yellow with rock powder layer |
| MC | 6°54'9" S, 113°4'49" E | 60.9 | 85 | Dolomite | Silty clay | Red |
| KA | 3°57'21" S, 122°14'59" E | 120 | 120 | Basalt | Silty clay | Yellowish-brown with purplish-red iron layer |
| KC | 3°35'34" S, 122°11'10" E | 20 | 150 | Basalt | Silty clay | |

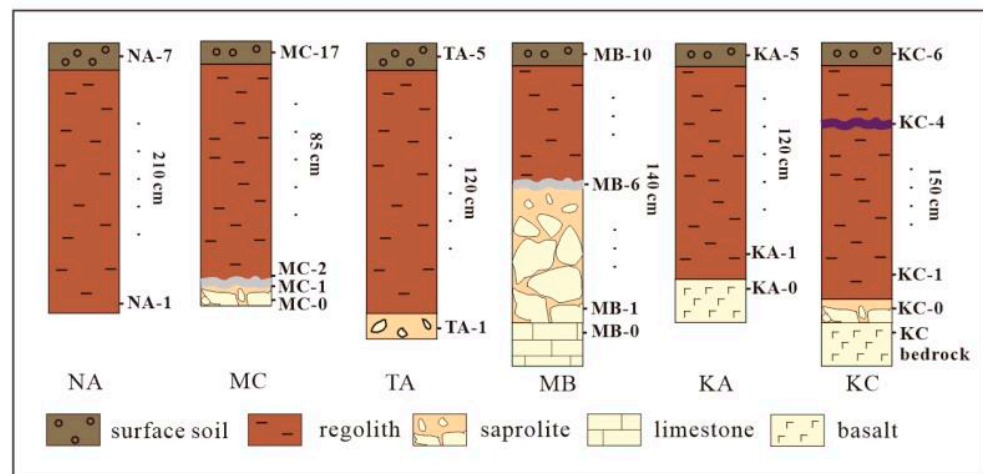


Figure 2. Studied soil profiles showing sectional structure and sampling depth of carbonate and basalt profiles taken from Indonesia.

2.3. Experimental and Chemical Analysis Methods

For the geochemical analysis, soil and bedrock samples were first ground by a ball mill and agate mortar and passed through a 75 μm sieve. Parameters including major, trace and rare earth elements were measured by Beijing Research Institute of Uranium Geology. The concentrations of major elements were determined by an X-ray fluorescence spectrograph (XRF) using the Philips PW2404 X-ray fluorescence spectrometer and the GB/T14506.28–93 silicate rock chemical analytical procedure. The contents of trace and rare earth elements were determined by inductively coupled plasma mass spectroscopy (HR-ICP-MS) (Element I, Finnigan MAT 110 Company, Waltham, MA, USA) based on the DZ/T0223-2001 ICP-MS procedure at a temperature of 20 °C and humidity of 30%. Initially, under closed conditions 0.1 g of powdered sample, 1.5 mL HF and 1 mL HNO₃ were added into a Teflon melting pot to dissolve the samples. At 140 °C the sample pot was heated for 48 h in a bake furnace, after which it was placed on an electrothermal plate for cooling and then 1 mL of HNO₃ was added. The procedure was repeated; then, 3 mL HNO₃ and 10 mL H₂O were added to dissolve the samples in a 100 mL plastic bottle for ICP-MS analysis. In using the neutron activation method, the analyses were checked against three standard samples. The analytical precision for major and trace elements was 1 and 10%, respectively. The soil pH values were determined by the People's Republic of China agricultural industry standard—soil pH determination (NY-T 1377-2007) [31]. The carbon contents of the soil samples were determined with a total organic carbon analyzer (liquid SOC II). Soil in our study was equivalent to Ultisols, Alfisols and Inceptisols based on soil taxonomy [32] and Acrisols, Lixisols, Luvisols and Nitisols in the World Reference Base for Soil Resources [7]. The dominant soil texture of the surface soil was determined to be silty clay.

2.4. Migration Coefficient

The migration coefficient, otherwise called mass balance calculation, is commonly used to assess the mobilization and distribution of elements during chemical weathering and pedogenesis processes [33–38]. The mass fraction elemental increase or decrease from soil during pedogenesis, relative to the mass initially present in the parent material, was calculated according to Equation (1) [39,40].

$$\text{mass balance of element } \tau_{ij} = \{[C_{j,w}/C_{j,p}]/[C_{i,w}/C_{i,p}]\} - 1 \quad (1)$$

where C is the concentration of the element j, w refers to the weathered material, p refers to the parent material, and i refers to the immobile reference element. The negative values of τ_{ij} indicate depletion of element and positive values indicate enrichment of element in the weathered profile. By referring to the “immobile plateau” method [41], Th was determined to be the least mobile element in our study, taking into consideration that normalizing Nb would produce similar results.

3. Results

3.1. Major Elements and Physiochemical Properties

Soil assessment and analysis were done for six clay-rich soil profiles in Indonesia. The results illustrated in Table 2 highlight major element contents, pH values and chemical index of alteration (CIA) variation with depth. In addition, average values from Upper Continental Crust (UCC), Post-Archean Australian Shale (PAAS), North American Shale Composite (NASC), and Average Loess Composition (AVL) were included for comparison.

The major element oxides result revealed a general enrichment in Fe, Al and Si contents and depletion in K and Na contents. The SiO₂ contents indicated high variability ranging from 4.12–76.5%, with the lowest value recorded in MB profile and the highest in NA soil profiles. The Al₂O₃ contents ranged from 1.18% in MB soil profile to 21.19% in MC soil profile. The highest Fe₂O₃ contents were recorded in the KA-KC profiles (16.29–46.12%) respectively. The low alkaline elemental oxides content of Na₂O and K₂O ranged from 0.01 to 0.04% and from <0.01 to 0.4%, respectively (Table 2).

Table 2. Major element contents and other relevant parameters in red soil weathering profiles within two districts in Indonesia.

| Profile | SiO ₂ | Al ₂ O ₃ | Fe ₂ O ₃ ^T | MgO | CaO | Na ₂ O | K ₂ O | MnO | TiO ₂ | P ₂ O ₅ | LOI | Total | pH | CIA | TOC |
|---------|------------------|--------------------------------|---|-------|-------|-------------------|------------------|------|------------------|-------------------------------|-------|-------|------|-------|-------|
| TA-5 | 13.81 | 3.70 | 1.74 | 12.28 | 27.88 | 0.09 | 0.10 | 0.05 | 0.20 | 0.78 | 39.33 | 99.96 | 7.36 | 89.87 | 14.25 |
| TA-4 | 10.88 | 2.85 | 1.38 | 12.60 | 30.36 | 0.05 | 0.07 | 0.04 | 0.16 | 0.75 | 40.85 | 99.99 | 7.32 | 92.11 | 14.24 |
| TA-3 | 13.29 | 3.47 | 1.68 | 12.08 | 29.07 | 0.06 | 0.09 | 0.05 | 0.19 | 0.84 | 39.09 | 99.91 | 7.22 | 91.97 | 14.22 |
| TA-2 | 20.21 | 5.30 | 2.64 | 9.83 | 24.78 | 0.08 | 0.12 | 0.08 | 0.29 | 1.29 | 35.30 | 99.92 | 7.15 | 92.58 | 12.92 |
| TA-1 | 27.91 | 7.89 | 3.85 | 7.63 | 19.39 | 0.12 | 0.17 | 0.11 | 0.40 | 1.43 | 31.07 | 99.97 | 7.15 | 92.74 | 11.74 |
| TA-0 | 1.04 | 0.11 | 0.06 | 8.90 | 44.48 | 0.02 | 0.02 | 0.00 | 0.02 | 0.09 | 44.71 | 99.45 | - | 60.29 | - |
| MB-10 | 36.45 | 11.69 | 5.23 | 0.56 | 19.50 | 0.07 | 0.32 | 0.08 | 0.68 | 0.08 | 25.26 | 99.92 | 7.36 | 95.00 | 4.61 |
| MB-9 | 20.00 | 7.51 | 3.05 | 0.41 | 34.68 | 0.03 | 0.20 | 0.05 | 0.41 | 0.05 | 33.57 | 99.96 | 7.36 | 95.82 | 7.49 |
| MB-8 | 18.41 | 6.75 | 2.61 | 0.40 | 36.47 | 0.02 | 0.19 | 0.05 | 0.38 | 0.05 | 34.66 | 99.99 | 7.34 | 95.92 | 8.70 |
| MB-7 | 13.50 | 4.76 | 1.83 | 0.34 | 41.96 | 0.02 | 0.14 | 0.04 | 0.28 | 0.04 | 37.02 | 99.93 | 7.33 | 95.34 | 7.48 |
| MB-6 | 11.57 | 3.05 | 1.13 | 0.40 | 45.19 | 0.02 | 0.15 | 0.02 | 0.21 | 0.03 | 38.00 | 99.77 | 7.43 | 93.11 | 6.09 |
| MB-5 | 13.45 | 3.87 | 1.40 | 0.43 | 43.03 | 0.02 | 0.18 | 0.02 | 0.26 | 0.03 | 37.22 | 99.91 | 7.41 | 93.15 | 6.05 |
| MB-4 | 4.12 | 1.18 | 0.46 | 0.39 | 51.74 | 0.02 | 0.08 | 0.01 | 0.08 | 0.02 | 41.33 | 99.43 | 7.58 | 88.18 | 4.72 |
| MB-3 | 13.19 | 3.83 | 1.42 | 0.41 | 43.03 | 0.02 | 0.17 | 0.03 | 0.25 | 0.03 | 37.55 | 99.93 | 7.36 | 93.26 | 6.76 |
| MB-2 | 14.85 | 3.92 | 1.38 | 0.46 | 42.34 | 0.03 | 0.22 | 0.02 | 0.25 | 0.03 | 36.46 | 99.96 | 7.38 | 91.77 | 5.89 |
| MB-1 | 11.51 | 2.95 | 1.03 | 0.39 | 45.43 | 0.02 | 0.18 | 0.02 | 0.20 | 0.02 | 38.07 | 99.82 | 7.43 | 91.59 | 5.81 |
| MB-0 | <0.010 | 0.02 | 0.03 | 0.72 | 55.10 | 0.03 | <0.010 | 0.00 | 0.01 | 0.01 | 43.49 | 99.41 | - | 18.24 | - |
| MC-0 | 0.18 | 0.11 | 0.10 | 20.13 | 32.53 | 0.02 | <0.010 | 0.00 | 0.02 | 0.12 | 46.21 | 99.42 | - | 61.41 | - |
| MC-1 | 1.36 | 0.61 | 0.40 | 19.07 | 32.28 | 0.01 | 0.01 | 0.01 | 0.05 | 0.20 | 45.43 | 99.43 | - | 91.04 | - |
| MC-2 | 54.00 | 20.74 | 11.83 | 0.24 | 0.28 | 0.02 | 0.04 | 0.12 | 1.27 | 0.31 | 11.14 | 99.99 | 7.34 | 99.46 | 0.35 |
| MC-3 | 54.54 | 20.64 | 11.52 | 0.21 | 0.23 | 0.02 | 0.04 | 0.12 | 1.26 | 0.31 | 11.07 | 99.96 | 7.07 | 99.38 | 0.32 |
| MC-4 | 54.30 | 20.68 | 11.58 | 0.21 | 0.23 | 0.02 | 0.04 | 0.13 | 1.27 | 0.30 | 11.18 | 99.94 | 6.86 | 99.43 | 0.33 |
| MC-5 | 54.16 | 20.78 | 11.75 | 0.23 | 0.23 | 0.03 | 0.04 | 0.14 | 1.28 | 0.30 | 11.05 | 99.99 | 6.75 | 99.38 | 0.33 |
| MC-6 | 54.15 | 20.72 | 11.69 | 0.22 | 0.27 | 0.02 | 0.04 | 0.13 | 1.27 | 0.30 | 11.15 | 99.96 | 6.58 | 99.41 | 0.36 |
| MC-7 | 55.71 | 20.22 | 11.24 | 0.21 | 0.23 | 0.04 | 0.04 | 0.13 | 1.21 | 0.27 | 10.61 | 99.91 | 6.20 | 99.10 | 0.38 |
| MC-8 | 56.03 | 19.93 | 11.26 | 0.23 | 0.27 | 0.04 | 0.04 | 0.11 | 1.24 | 0.28 | 10.43 | 99.86 | 6.23 | 99.06 | 0.43 |
| MC-9 | 56.48 | 19.63 | 11.05 | 0.21 | 0.28 | 0.03 | 0.04 | 0.12 | 1.19 | 0.30 | 10.54 | 99.87 | 6.23 | 99.30 | 0.46 |
| MC-10 | 56.08 | 19.91 | 11.23 | 0.23 | 0.24 | 0.03 | 0.04 | 0.12 | 1.20 | 0.28 | 10.51 | 99.87 | 6.30 | 99.32 | 0.51 |
| MC-11 | 56.45 | 19.66 | 11.08 | 0.22 | 0.25 | 0.02 | 0.04 | 0.12 | 1.19 | 0.28 | 10.62 | 99.93 | 6.32 | 99.39 | 0.43 |
| MC-12 | 54.79 | 20.57 | 11.48 | 0.23 | 0.26 | 0.03 | 0.04 | 0.13 | 1.23 | 0.28 | 10.89 | 99.93 | 6.28 | 99.32 | 0.39 |
| MC-13 | 53.93 | 20.76 | 11.66 | 0.26 | 0.29 | 0.03 | 0.04 | 0.13 | 1.26 | 0.28 | 11.23 | 99.87 | 6.44 | 99.34 | 0.41 |
| MC-14 | 53.22 | 21.11 | 11.87 | 0.27 | 0.30 | 0.03 | 0.04 | 0.13 | 1.27 | 0.28 | 11.46 | 99.98 | 6.43 | 99.36 | 0.42 |
| MC-15 | 53.10 | 21.08 | 12.10 | 0.27 | 0.29 | 0.03 | 0.03 | 0.13 | 1.26 | 0.28 | 11.37 | 99.94 | 6.44 | 99.39 | 0.37 |
| MC-16 | 53.37 | 20.97 | 11.71 | 0.34 | 0.42 | 0.02 | 0.04 | 0.12 | 1.26 | 0.29 | 11.42 | 99.96 | 6.59 | 99.43 | 0.36 |
| MC-17 | 53.17 | 21.19 | 12.00 | 0.27 | 0.30 | 0.02 | 0.04 | 0.12 | 1.31 | 0.31 | 11.15 | 99.88 | 6.51 | 99.46 | 0.00 |
| NA-0 | 0.25 | 0.19 | 0.11 | 8.31 | 45.75 | 0.01 | <0.010 | 0.02 | 0.02 | 0.11 | 44.66 | 99.43 | - | 79.49 | - |

Table 2. Cont.

| Profile | SiO ₂ | Al ₂ O ₃ | Fe ₂ O ₃ ^T | MgO | CaO | Na ₂ O | K ₂ O | MnO | TiO ₂ | P ₂ O ₅ | LOI | Total | pH | CIA | TOC |
|-------------------|------------------|--------------------------------|---|-------|------|-------------------|------------------|------|------------------|-------------------------------|-------|-------|------|-------|------|
| NA-7 | 72.28 | 12.53 | 5.97 | 0.23 | 0.22 | 0.03 | 0.38 | 0.05 | 0.63 | 0.05 | 7.53 | 99.9 | 5.36 | 95.75 | 0.43 |
| NA-6 | 71.94 | 12.68 | 6.28 | 0.21 | 0.20 | 0.03 | 0.38 | 0.04 | 0.65 | 0.06 | 7.49 | 99.96 | 5.34 | 95.82 | 0.42 |
| NA-5 | 72.28 | 12.62 | 6.36 | 0.19 | 0.20 | 0.04 | 0.34 | 0.02 | 0.64 | 0.06 | 7.16 | 99.91 | 5.31 | 96.10 | 0.30 |
| NA-4 | 74.03 | 11.55 | 6.09 | 0.19 | 0.18 | 0.03 | 0.32 | 0.02 | 0.62 | 0.06 | 6.86 | 99.95 | 5.27 | 96.05 | 0.23 |
| NA-3 | 72.52 | 10.90 | 8.36 | 0.18 | 0.17 | 0.04 | 0.32 | 0.05 | 0.64 | 0.06 | 6.75 | 99.99 | 5.22 | 95.74 | 0.11 |
| NA-2 | 71.20 | 10.68 | 9.86 | 0.20 | 0.27 | 0.04 | 0.35 | 0.03 | 0.66 | 0.06 | 6.63 | 99.98 | 5.18 | 95.32 | 0.10 |
| NA-1 | 76.50 | 10.06 | 6.31 | 0.18 | 0.15 | 0.04 | 0.40 | 0.02 | 0.70 | 0.04 | 5.52 | 99.92 | 4.98 | 94.50 | 0.10 |
| KA-0 | 51.60 | 6.47 | 7.63 | 23.08 | 9.53 | 0.31 | <0.010 | 0.30 | 0.08 | 0.01 | 0.40 | 99.41 | - | 85.53 | - |
| KA-1 | 49.10 | 1.67 | 16.29 | 15.29 | 0.86 | <0.010 | <0.010 | 0.23 | 0.03 | 0.01 | 15.94 | 99.42 | 5.50 | 97.30 | 0.00 |
| KA-2 | 50.63 | 1.26 | 16.41 | 14.20 | 0.61 | 0.01 | <0.010 | 0.25 | 0.02 | 0.01 | 16.09 | 99.49 | 5.43 | 96.45 | 0.00 |
| KA-3 | 53.41 | 3.12 | 21.94 | 5.62 | 0.27 | 0.03 | 0.01 | 0.13 | 0.08 | 0.02 | 14.78 | 99.41 | 5.43 | 96.21 | 1.27 |
| KA-4 | 53.19 | 2.82 | 20.69 | 7.72 | 0.43 | 0.02 | 0.01 | 0.17 | 0.07 | 0.02 | 14.25 | 99.39 | 5.32 | 96.74 | 0.80 |
| KA-5 | 62.76 | 2.59 | 19.07 | 4.13 | 0.23 | 0.01 | 0.01 | 0.14 | 0.07 | 0.02 | 10.39 | 99.42 | 5.17 | 97.73 | 1.09 |
| KC-rock | 38.84 | 0.13 | 9.11 | 38.80 | 0.10 | <0.010 | <0.010 | 0.12 | 0.01 | 0.01 | 12.61 | 99.73 | - | 72.96 | - |
| KC-0 | 42.90 | 1.90 | 12.48 | 34.68 | 1.20 | <0.010 | <0.010 | 0.17 | 0.03 | 0.01 | 4.59 | 97.96 | 7.36 | 97.62 | 0.00 |
| KC-1 | 21.77 | 17.34 | 39.64 | 0.95 | 0.04 | <0.010 | <0.010 | 1.16 | 0.41 | 0.02 | 16.07 | 97.4 | 4.96 | 99.73 | 0.04 |
| KC-2 | 15.80 | 16.69 | 46.12 | 0.94 | 0.05 | 0.01 | <0.010 | 0.83 | 0.47 | 0.02 | 15.96 | 96.89 | 5.17 | 99.70 | 0.07 |
| KC-3 | 19.51 | 17.83 | 41.74 | 1.00 | 0.04 | 0.01 | <0.010 | 0.62 | 0.41 | 0.02 | 16.19 | 97.37 | 4.96 | 99.68 | 0.03 |
| KC-4 | 23.10 | 18.43 | 39.28 | 0.39 | 0.04 | 0.01 | <0.010 | 0.67 | 0.41 | 0.01 | 15.40 | 97.74 | 4.61 | 99.75 | 0.03 |
| KC-5 | 17.04 | 18.30 | 42.41 | 1.29 | 0.04 | 0.01 | <0.010 | 0.62 | 0.51 | 0.02 | 16.71 | 96.95 | 5.13 | 99.75 | 0.10 |
| KC-6 | 18.02 | 17.43 | 42.47 | 1.88 | 0.04 | 0.02 | <0.010 | 0.48 | 0.53 | 0.02 | 16.93 | 97.82 | 5.25 | 99.56 | 0.06 |
| UCC ^a | 66.62 | 15.40 | 5.04 | 2.48 | 3.59 | 3.27 | 2.80 | 0.10 | 0.64 | 0.15 | - | - | - | - | - |
| PAAS ^b | 62.8 | 18.9 | 7.22 | 2.2 | 1.3 | 1.2 | 3.7 | 0.11 | 1 | 0.16 | - | - | - | - | - |
| NASC ^c | 64.8 | 16.9 | 5.65 | 2.2 | 3.63 | 1.14 | 3.97 | 0.06 | 0.7 | 0.13 | - | - | - | - | - |
| AVL ^d | 71.19 | 11.63 | 3.68 | 2.86 | 6.46 | 1.69 | 2.21 | 0.07 | 0.69 | 0.14 | - | - | - | - | - |

Major element oxides measured in (wt%). UCC^a: Average of Upper Continental Crust [42]. PAAS^b: Post-Archean Australian Shale [43]. NASC^c: North American Shale Composite [44]. AVL^d: Average Loess Composition [45]. CIA = (Al₂O₃/Al₂O₃ + CaO + Na₂O + K₂O) × 100. LOI = loss on ignition. TOC = total organic carbon g kg⁻¹. The symbol (-) indicates values below detection limit (less than 0.001) b.

The pH values for the six red soil profiles varied with depth and ranged between 4.61 and 7.58 (Table 2). The profiles can be divided into three groups based on pH value range: alkaline with pH values >7 (TA-MB; limestone), slightly acidic with pH values 6–6.9 (MC-NA; dolomite), and acidic with pH values <5.5 (KA-KC; basalt).

The CIA values for the six red soil profiles ranged from 88.76–99.76 (Table 2) and indicated a distinct trend with depth. The lowest average CIA values were reported in TA-MB soil profiles (93.2), while the highest were recorded in KA-KC soil profiles (98.5).

3.2. Trace Element Distribution

The trace element contents within the six red soil profiles are given in Table 3. In addition, the normalized UCC spider diagram of the samples is shown in Figure 3a–f. Similar trace element distribution and behavioral trends were observed for the limestone profiles (TA-MB) with strong depletion in Be and Rb, while Cd was enriched (Figure 3a,b). The basalt profiles (KA-KC) showed the greatest fluctuation when compared to the normalized UCC spider values (Figure 3c,d) with strong depletion in Li, Be, Rb and Sr, while strong enrichment in Cr, Co, Cu and Ni can be seen. The dolomite profiles (MC-NA) showed similar distribution and behavior in trace elements when compared to the normalized UCC spider diagram (Figure 3e,f), with depletion in Be, Ni, Rb, Sr and slight enrichment in the others. The trace elements in the samples indicate similar element distribution patterns with their bedrocks, however the basalt profiles (KA-KC) indicated high variation when compared to UCC normalized values. Conversely, the KA bedrock value for elements Sc, V, Ga and Y was larger than the regolith values. The carbonate bedrock profiles (TA-MB; MC-NA) containing high concentration of Sr were vastly different from those of basalt bedrocks (KA-KC) with high concentration of Cr and Ni.

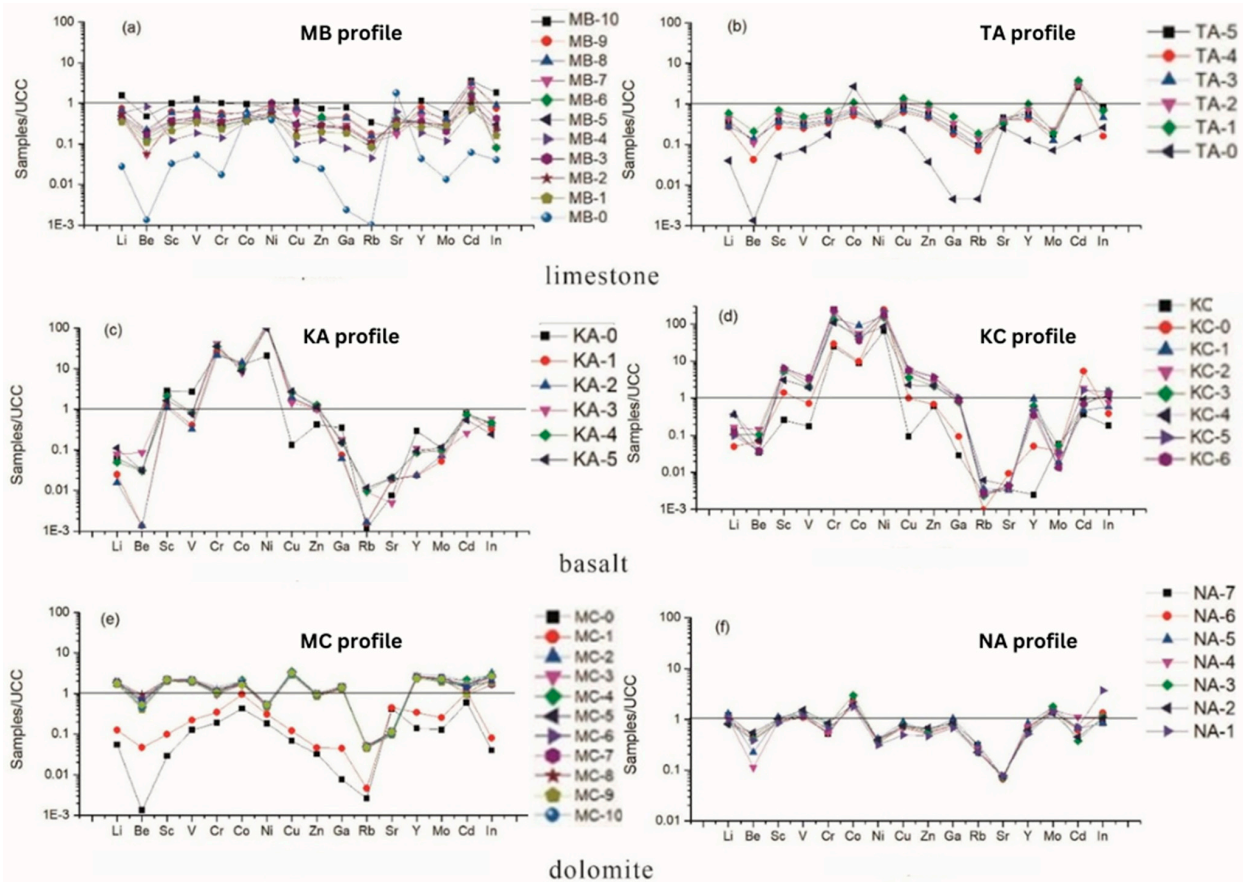


Figure 3. Trace elements, bedrock sample and UCC normalized spider diagrams for six red soil profiles within two districts in Indonesia. (a,b) Limestone-based profiles (MB-TA), (c,d) basalt-based profiles (KA-KC) and (e,f) dolomite-based profiles (MC-NA). The UCC values are from [43].

Table 3. Trace element concentrations from six red soil weathering profiles within two districts in Indonesia.

| Samples | MC-0 | MC-1 | MC-2 | MC-3 | MC-4 | MC-5 | MC-6 | MC-7 | MC-8 | MC-9 | MC-10 | MC-11 | MC-12 |
|---------|--------|-------|-------|-------|-------|-------|-------|-------|-------|-------|---------|-------|-------|
| Li | 1.1 | 2.5 | 34.1 | 38 | 36.5 | 38.3 | 39.6 | 37.2 | 39.1 | 33.9 | 35.9 | 38.7 | 34.3 |
| Be | 0.004 | 0.14 | 1.8 | 1.91 | 1.39 | 2.35 | 1.83 | 1.95 | 2.87 | 1.21 | 1.34 | 1.49 | 2 |
| Sc | 0.395 | 1.34 | 28.1 | 31.1 | 29.8 | 29.7 | 30.4 | 27.3 | 30.5 | 27.4 | 28.2 | 28.5 | 27.6 |
| V | 13.6 | 23.6 | 225 | 225 | 226 | 229 | 233 | 205 | 232 | 198 | 209 | 218 | 224 |
| Cr | 16.2 | 29.4 | 102 | 82.1 | 97.4 | 94.4 | 82.4 | 96 | 102 | 84.7 | 87.9 | 96.4 | 104 |
| Co | 7.2 | 16.3 | 30.5 | 27.5 | 36.4 | 29.7 | 30.6 | 29.2 | 33.6 | 29.2 | 34.3 | 33.1 | 33.4 |
| Ni | 8.07 | 13.5 | 22.8 | 22.9 | 23.2 | 23.1 | 24 | 21 | 23.3 | 20.1 | 21.7 | 22.9 | 23.6 |
| Cu | 1.7 | 3.02 | 78.3 | 80 | 87.1 | 81.3 | 83.2 | 73.9 | 81.1 | 69.8 | 73.9 | 77.3 | 79.3 |
| Zn | 2.29 | 3.29 | 64.8 | 68.7 | 68.2 | 69.6 | 71.1 | 62.4 | 67.8 | 59.1 | 64.1 | 65.3 | 64.3 |
| Ga | 0.129 | 0.763 | 23.4 | 24.5 | 24.8 | 24.6 | 24.7 | 22.9 | 25.2 | 21.6 | 23.2 | 23.6 | 23.9 |
| Rb | 0.294 | 0.517 | 5.66 | 5.92 | 5.69 | 5.54 | 5.74 | 5.08 | 5.64 | 5 | 5.34 | 5.43 | 5.37 |
| Sr | 147 | 155 | 39.4 | 40.7 | 40 | 38.9 | 41.2 | 34.3 | 39.5 | 33 | 34.4 | 36 | 36.8 |
| Y | 3.05 | 7.54 | 54.3 | 53.6 | 52.2 | 54.5 | 56.4 | 53.8 | 60.5 | 51.1 | 54.6 | 56.3 | 55.7 |
| Mo | 0.191 | 0.381 | 3.19 | 3.19 | 3.34 | 3.6 | 2.95 | 3.53 | 3.41 | 2.87 | 3.16 | 3.14 | 3.42 |
| Cd | 0.058 | 0.106 | 0.151 | 0.158 | 0.216 | 0.159 | 0.141 | 0.09 | 0.166 | 0.167 | 0.133 | 0.173 | 0.106 |
| In | <0.002 | 0.004 | 0.158 | 0.129 | 0.143 | 0.137 | 0.13 | 0.083 | 0.131 | 0.09 | 0.133 | 0.145 | 0.105 |
| Samples | MB-10 | MB-9 | MB-8 | MB-7 | MB-6 | MB-5 | MB-4 | MB-3 | MB-2 | MB-1 | MB-0 | TA-5 | TA-4 |
| Li | 30.6 | 15 | 13.6 | 8.44 | 8.12 | 9.87 | 11.5 | 8.66 | 10.6 | 7.03 | 0.553 | 7.33 | 5.36 |
| Be | 1.42 | 0.568 | 0.668 | 0.163 | 0.403 | 0.57 | 2.47 | 0.501 | 0.171 | 0.323 | 0.004 | 0.362 | 0.127 |
| Sc | 13.4 | 8.27 | 7.94 | 5.39 | 4.23 | 5.09 | 1.66 | 4.92 | 4.36 | 2.81 | 0.437 | 5.26 | 3.68 |
| V | 135 | 63.5 | 76 | 39.3 | 40.1 | 47.9 | 19.6 | 50.9 | 33.9 | 36.9 | 5.61 | 35.4 | 26.5 |
| Cr | 85.1 | 48.7 | 43.4 | 30.8 | 23.1 | 25.5 | 11.8 | 30.4 | 28.1 | 19.4 | 1.48 | 34.4 | 28.5 |
| Co | 16 | 9.47 | 10.4 | 7.63 | 7.05 | 6.27 | 6.11 | 7.94 | 8.2 | 6.29 | 8.79 | 12.1 | 8.52 |
| Ni | 36.5 | 36.3 | 30.3 | 23.1 | 21 | 19.7 | 27.1 | 45.1 | 24.6 | 18.4 | 16.9 | 14.4 | 13.2 |
| Cu | 27.1 | 18.9 | 18.6 | 14.1 | 7.15 | 8.23 | 2.47 | 7.4 | 5.31 | 3.81 | 1.02 | 21.2 | 15.4 |
| Zn | 51.8 | 31.7 | 29.7 | 19.3 | 32.7 | 18 | 8.97 | 20.8 | 20.6 | 13.8 | 1.71 | 40.3 | 31.7 |
| Ga | 13.2 | 7.86 | 7.34 | 4.88 | 3.26 | 4.01 | 1.33 | 4.09 | 4.35 | 3.08 | 0.04 | 4.29 | 2.97 |
| Rb | 38.1 | 19.6 | 17.5 | 11.9 | 9.14 | 11.3 | 4.96 | 11.7 | 12.9 | 9.54 | 0.114 | 10.7 | 7.89 |
| Sr | 80.5 | 68.7 | 68 | 59.6 | 146 | 122 | 216 | 128 | 115 | 102 | 625 | 160 | 140 |
| Y | 25.1 | 16.8 | 13.6 | 10.4 | 7.57 | 7.58 | 4.09 | 7.8 | 6.96 | 5.63 | 0.944 | 12.4 | 9.29 |
| Mo | 0.833 | 0.52 | 0.621 | 0.395 | 0.344 | 0.421 | 0.176 | 0.3 | 0.443 | 0.427 | 0.02 | 0.257 | 0.284 |
| Cd | 0.348 | 0.308 | 0.303 | 0.222 | 0.167 | 0.098 | 0.066 | 0.147 | 0.113 | 0.072 | 0.006 | 0.247 | 0.284 |
| In | 0.091 | 0.037 | 0.044 | 0.004 | 0.004 | 0.015 | 0.011 | 0.021 | 0.012 | 0.008 | <0.002 | 0.042 | 0.008 |
| Samples | TA-3 | TA-2 | TA-1 | TA-0 | KA-0 | KA-1 | KA-2 | KA-3 | KA-4 | KA-5 | KC-rock | KC-0 | KC-1 |
| Li | 5.57 | 8.72 | 11.7 | 0.799 | 1.25 | 0.488 | 0.312 | 1.56 | 0.982 | 2.19 | 2.88 | 0.979 | 7.24 |

Table 3. Cont.

| Samples | MC-0 | MC-1 | MC-2 | MC-3 | MC-4 | MC-5 | MC-6 | MC-7 | MC-8 | MC-9 | MC-10 | MC-11 | MC-12 |
|----------------|-------------|-------------|-------------|-------------|-------------|-------------|-------------|-------------|-------------|-------------|-------------|-------------|-------|
| Be | 0.414 | 0.322 | 0.632 | 0.004 | 0.093 | 0.004 | 0.004 | 0.256 | 0.092 | 0.093 | 0.103 | 0.206 | 0.108 |
| Sc | 4.82 | 7.32 | 9.51 | 0.7 | 38.7 | 16.8 | 14.8 | 28.5 | 28.3 | 22 | 3.46 | 18.8 | 73.3 |
| V | 30.4 | 44 | 51.7 | 8.13 | 287 | 42.8 | 34.8 | 89.2 | 85.8 | 81.3 | 18.5 | 76.6 | 221 |
| Cr | 31.1 | 42.4 | 54.7 | 14.9 | 2036 | 2276 | 1793 | 3528 | 3002 | 2991 | 2044 | 2433 | 12437 |
| Co | 10.5 | 12.8 | 18.2 | 45.4 | 210 | 223 | 240 | 136 | 170 | 148 | 149 | 164 | 1530 |
| Ni | 13.4 | 13.6 | 13.8 | 14.6 | 913 | 4443 | 5417 | 5128 | 5200 | 4287 | 2876 | 10873 | 7281 |
| Cu | 17.5 | 26.5 | 34.4 | 5.74 | 3.28 | 45 | 47.9 | 35.9 | 65.6 | 68.9 | 2.27 | 24.8 | 133 |
| Zn | 34.6 | 53.2 | 69.6 | 2.65 | 29.3 | 70.5 | 72.2 | 72.3 | 90.8 | 80.7 | 42.9 | 48 | 187 |
| Ga | 3.49 | 5.53 | 8.26 | 0.077 | 5.89 | 1.25 | 1.04 | 2.98 | 2.54 | 2.58 | 0.48 | 1.56 | 16.3 |
| Rb | 10.2 | 15.7 | 20.7 | 0.514 | 0.13 | 0.172 | 0.183 | 1.03 | 1.06 | 1.31 | 0.286 | 0.108 | 0.404 |
| Sr | 144 | 131 | 112 | 87.9 | 2.63 | 6.33 | 6.68 | 1.71 | 7.26 | 7.2 | 1.2 | 3.2 | 1.14 |
| Y | 10.8 | 15.8 | 21.9 | 2.75 | 6.35 | 0.511 | 0.512 | 2.39 | 1.86 | 2.05 | 0.054 | 1.1 | 21 |
| Mo | 0.191 | 0.344 | 0.287 | 0.108 | 0.162 | 0.078 | 0.107 | 0.127 | 0.148 | 0.173 | 0.087 | 0.057 | 0.028 |
| Cd | 0.325 | 0.3 | 0.367 | 0.014 | 0.077 | 0.073 | 0.074 | 0.025 | 0.072 | 0.053 | 0.035 | 0.518 | 0.046 |
| In | 0.023 | 0.034 | 0.034 | 0.013 | 0.022 | 0.016 | 0.021 | 0.029 | 0.023 | 0.012 | 0.009 | 0.019 | 0.029 |
| Samples | KC-2 | KC-3 | KC-4 | KC-5 | KC-6 | NA-7 | NA-6 | NA-5 | NA-4 | NA-3 | NA-2 | NA-1 | |
| Li | 3.25 | 2.07 | 7.26 | 1.91 | 2.37 | 24.1 | 21.4 | 25.7 | 20.8 | 16.4 | 15.9 | 19.6 | |
| Be | 0.422 | 0.31 | 0.217 | 0.115 | 0.114 | 1.38 | 1.21 | 0.664 | 0.336 | 1.2 | 1.64 | 1.14 | |
| Sc | 81.6 | 73.2 | 41.7 | 89.7 | 86 | 13.4 | 12.3 | 14.9 | 12.3 | 11.9 | 13.7 | 11.4 | |
| V | 296 | 221 | 209 | 374 | 375 | 127 | 115 | 138 | 125 | 146 | 163 | 124 | |
| Cr | 16553 | 10888 | 9204 | 18540 | 21714 | 43.8 | 46.6 | 52.4 | 46.7 | 66.8 | 71.5 | 55.8 | |
| Co | 932 | 661 | 795 | 754 | 591 | 38.5 | 36.2 | 33 | 34.9 | 49.9 | 32.3 | 29.5 | |
| Ni | 8931 | 6667 | 3754 | 9649 | 7506 | 17.9 | 15.3 | 18.2 | 16.3 | 16 | 17.1 | 13.6 | |
| Cu | 123 | 90 | 56.6 | 153 | 141 | 18.1 | 17.1 | 21.8 | 17.3 | 18.6 | 18.4 | 12.2 | |
| Zn | 189 | 151 | 152 | 265 | 255 | 45.3 | 39.6 | 41.4 | 35.3 | 40.4 | 48 | 32.7 | |
| Ga | 15.4 | 13.2 | 14.2 | 17.1 | 14.5 | 14.3 | 12.7 | 17.3 | 12.9 | 13 | 13.8 | 11.4 | |
| Rb | 0.281 | 0.26 | 0.681 | 0.273 | 0.306 | 35.3 | 29.8 | 35.2 | 29.2 | 25.1 | 24.8 | 25.4 | |
| Sr | 1.37 | 1.51 | 1.51 | 1.55 | 1.49 | 24.8 | 23 | 25.6 | 25.3 | 24.9 | 26.4 | 27 | |
| Y | 11.9 | 13.4 | 10.4 | 10.4 | 7.4 | 15.2 | 15.1 | 18.1 | 15.7 | 12.7 | 13.1 | 11.2 | |
| Mo | 0.042 | 0.079 | 0.02 | 0.052 | 0.02 | 2.1 | 2.2 | 2.61 | 2.29 | 2.66 | 1.96 | 2.11 | |
| Cd | 0.181 | 0.066 | 0.09 | 0.159 | 0.068 | 0.064 | 0.059 | 0.065 | 0.109 | 0.037 | 0.044 | 0.068 | |
| In | 0.039 | 0.076 | 0.054 | 0.076 | 0.063 | 0.042 | 0.066 | 0.042 | 0.054 | 0.056 | 0.052 | 0.185 | |

All the trace element values are in ppm.

3.3. Rare Earth Element (REE) Distribution

The concentrations of REEs and other parameters taken for six red soil profiles are listed in Table 4. The total REEs varied remarkably among the studied soil profiles with values ranging from 0.635–256.56 ppm. The basalt profiles (KA-KC) had the lowest values while dolomite profiles (MC-NA) had the highest values. A similar trend recorded for the total REEs in the underlying bedrock ranged from 0.237–6.447 ppm. The spider diagram for the carbonate profiles (TA-MB; MC-NA) revealed a similar incline shape towards the right, characterized by a steep light rare earth element (LREE) fraction and relatively flat heavy rare earth element (HREE) (Figure 4). There was slight depletion in Eu for both profiles while a positive Ce anomaly existed in the lower section of the NA soil profile. Conversely, the spider diagram for the basalt profiles (KA-KC) was relatively flat with no obvious difference between LREE and HREE for the regolith, except for the bedrock sample. The KA soil profile, however, showed depletion in Ce and Gd while the KC profile indicated depletion in Ce and Eu (Figure 4).

3.4. Migration Coefficient

According to the elemental migration coefficient using $\tau_{Th, j}$ as the reference element, the major elements indicated variability with depth for the soil profiles (Figure 5a,b). The general trend indicated enrichment in Si, Al and Fe for the carbonate profiles; however, the basalt profiles KA and KC indicated depletion in Al and depletion in Si and Fe, respectively (Figure 5a). The other major elements (Mg, Ca, Na, K, Mn, P) indicated depletion throughout the entire carbonate profiles, while KA, KC and NA profiles indicated variability in enrichment and depletion of preferential major elements at different sections of the profiles (Figure 5b). The transitional elements (Zn, Cu, Co, Ni, Cr) showed relatively constant depletion throughout the entire carbonate profiles, except for NA profile (Figure 6). Conversely, the basalt profiles (KA-KC) indicated enrichment and depletion in certain transitional elements (Figure 6). The transitional elements indicated a similar behavioral pattern with some major elements and REEs. The REEs, otherwise known as lanthanide elements, i.e., La-Lu, further separated into LREE (La-Dy) and HREE (Gd-Lu), indicating variability in the migration coefficient among the profiles (Figure 7). The general trend indicated significant depletion in all LREE throughout the entire profile for carbonate profiles with similar migration coefficients. Conversely, there was enrichment of LREE for the basalt profiles (KA, KC) and NA profile, except for the element Dy in the KA profile, Ce in the KC profile and in the upper section of the NA profile (Figure 7a). On the other hand, the carbonate profiles (TA, MB, MC) and KA profile indicated significant depletion in HREE throughout the entire profiles, with enrichment for KC and NA soil profiles (Figure 7b). In addition, there was a noticeable drastic change in the migration coefficient from bedrock to regolith, with small variation throughout the limestone profiles. The migration coefficient in the lower section of the MC profile increased slightly and then decreased sharply, which may be due to the existence of a rock powder layer.

Table 4. Rare earth contents and other relevant parameters from six typical red soil profiles within two districts in Indonesia.

| Samples | MC-0 | MC-1 | MC-2 | MC-3 | MC-4 | MC-5 | MC-6 | MC-7 | MC-8 | MC-9 | MC-10 | MC-11 | MC-12 |
|----------------------|-------|-------|--------|--------|--------|--------|--------|--------|--------|--------|--------|--------|--------|
| La | 1.20 | 3.04 | 45.10 | 46.60 | 46.20 | 45.80 | 48.20 | 41.30 | 44.70 | 39.10 | 42.50 | 43.40 | 43.20 |
| Ce | 1.32 | 3.83 | 77.90 | 80.40 | 79.40 | 80.40 | 83.80 | 74.00 | 81.20 | 70.10 | 76.80 | 78.10 | 78.90 |
| Pr | 0.29 | 0.77 | 11.30 | 11.70 | 11.70 | 11.40 | 11.90 | 10.20 | 11.30 | 9.77 | 10.50 | 10.90 | 10.90 |
| Nd | 1.32 | 3.45 | 47.30 | 48.50 | 48.70 | 48.10 | 50.00 | 43.40 | 48.30 | 41.90 | 44.20 | 45.50 | 46.40 |
| Sm | 0.31 | 0.80 | 10.40 | 10.60 | 10.70 | 10.40 | 11.00 | 9.68 | 10.70 | 9.07 | 9.81 | 10.50 | 10.30 |
| Eu | 0.08 | 0.21 | 2.60 | 2.58 | 2.68 | 2.68 | 2.87 | 2.53 | 2.79 | 2.35 | 2.52 | 2.61 | 2.60 |
| Gd | 0.49 | 1.20 | 9.11 | 9.94 | 9.31 | 8.97 | 10.40 | 9.61 | 10.30 | 8.80 | 9.00 | 10.40 | 8.95 |
| Tb | 0.06 | 0.18 | 1.53 | 1.44 | 1.56 | 1.56 | 1.56 | 1.60 | 1.72 | 1.34 | 1.56 | 1.55 | 1.44 |
| Dy | 0.39 | 1.01 | 9.97 | 9.48 | 9.89 | 9.80 | 10.40 | 9.57 | 10.90 | 9.46 | 10.10 | 9.88 | 10.30 |
| Ho | 0.09 | 0.17 | 1.95 | 1.91 | 1.85 | 2.12 | 1.95 | 1.95 | 2.07 | 1.85 | 1.99 | 1.97 | 1.95 |
| Er | 0.24 | 0.59 | 5.59 | 5.77 | 5.69 | 5.38 | 5.83 | 4.81 | 5.74 | 5.38 | 5.27 | 5.79 | 5.89 |
| Tm | 0.01 | 0.10 | 1.21 | 1.06 | 1.10 | 1.00 | 1.16 | 1.10 | 1.09 | 1.17 | 1.15 | 1.15 | 1.06 |
| Yb | 0.28 | 0.83 | 5.92 | 6.81 | 6.07 | 6.15 | 7.11 | 5.49 | 6.30 | 5.66 | 5.84 | 6.89 | 6.10 |
| Lu | 0.03 | 0.09 | 1.00 | 0.87 | 0.89 | 0.94 | 0.87 | 0.98 | 1.03 | 0.85 | 1.02 | 0.99 | 0.94 |
| LREE | 4.52 | 12.10 | 194.60 | 200.38 | 199.38 | 198.78 | 207.77 | 181.11 | 198.99 | 172.29 | 186.33 | 191.01 | 192.30 |
| HREE | 1.59 | 4.17 | 36.28 | 37.28 | 36.36 | 35.92 | 39.28 | 35.11 | 39.15 | 34.51 | 35.93 | 38.62 | 36.63 |
| LREE/HREE | 2.84 | 2.90 | 5.36 | 5.37 | 5.48 | 5.53 | 5.29 | 5.16 | 5.08 | 4.99 | 5.19 | 4.95 | 5.25 |
| ΣREE | 6.10 | 16.27 | 230.88 | 237.66 | 235.74 | 234.70 | 247.05 | 216.22 | 238.14 | 206.80 | 222.26 | 229.63 | 228.93 |
| δCe | 0.54 | 0.60 | 0.83 | 0.83 | 0.82 | 0.85 | 0.84 | 0.87 | 0.87 | 0.86 | 0.88 | 0.86 | 0.88 |
| δEu | 0.51 | 0.59 | 1.21 | 1.18 | 1.20 | 1.26 | 1.18 | 1.16 | 1.17 | 1.18 | 1.23 | 1.13 | 1.24 |
| (La/Yb) _N | 1.71 | 1.44 | 3.00 | 2.69 | 3.00 | 2.93 | 2.67 | 2.96 | 2.79 | 2.72 | 2.86 | 2.48 | 2.79 |
| (La/Sm) _N | 1.53 | 1.50 | 1.71 | 1.73 | 1.70 | 1.73 | 1.72 | 1.68 | 1.64 | 1.70 | 1.70 | 1.63 | 1.65 |
| (Gd/Yb) _N | 1.77 | 1.44 | 1.54 | 1.46 | 1.53 | 1.46 | 1.46 | 1.75 | 1.63 | 1.55 | 1.54 | 1.51 | 1.47 |
| Samples | MC-13 | MC-14 | MC-15 | MC-16 | MC-17 | NA-7 | NA-6 | NA-5 | NA-4 | NA-3 | NA-2 | NA-1 | NA-0 |
| La | 43.90 | 46.20 | 48.70 | 47.80 | 50.90 | 19.50 | 18.10 | 21.70 | 17.80 | 17.60 | 17.90 | 17.50 | 1.32 |
| Ce | 80.80 | 83.10 | 87.30 | 81.60 | 87.70 | 40.00 | 36.20 | 41.30 | 38.00 | 78.60 | 89.50 | 46.80 | 1.41 |
| Pr | 11.00 | 11.80 | 12.30 | 11.90 | 12.30 | 4.54 | 4.40 | 5.55 | 4.52 | 4.33 | 4.43 | 3.90 | 0.31 |
| Nd | 46.60 | 50.20 | 52.60 | 50.50 | 51.60 | 17.80 | 18.00 | 22.60 | 18.50 | 16.90 | 17.10 | 15.10 | 1.46 |
| Sm | 10.30 | 11.00 | 11.50 | 11.00 | 10.80 | 3.52 | 3.69 | 5.54 | 3.75 | 3.46 | 3.52 | 2.75 | 0.31 |
| Eu | 2.60 | 2.82 | 3.06 | 2.74 | 2.59 | 0.83 | 0.87 | 1.24 | 0.89 | 0.77 | 0.80 | 0.58 | 0.06 |
| Gd | 9.25 | 10.10 | 10.70 | 10.20 | 8.55 | 2.95 | 2.27 | 4.81 | 3.15 | 2.32 | 2.89 | 2.21 | 0.40 |
| Tb | 1.61 | 1.65 | 1.67 | 1.49 | 1.50 | 0.39 | 0.47 | 0.66 | 0.50 | 0.39 | 0.40 | 0.30 | 0.08 |
| Dy | 9.88 | 10.80 | 11.10 | 10.70 | 9.64 | 2.96 | 3.09 | 4.67 | 3.23 | 2.71 | 2.82 | 2.36 | 0.33 |
| Ho | 1.96 | 2.14 | 2.31 | 2.13 | 1.88 | 0.56 | 0.54 | 0.77 | 0.58 | 0.56 | 0.53 | 0.47 | 0.08 |
| Er | 5.35 | 5.70 | 6.04 | 5.92 | 5.21 | 1.78 | 1.58 | 2.13 | 1.68 | 1.48 | 1.32 | 1.44 | 0.17 |

Table 4. Cont.

| Samples | MC-0 | MC-1 | MC-2 | MC-3 | MC-4 | MC-5 | MC-6 | MC-7 | MC-8 | MC-9 | MC-10 | MC-11 | MC-12 |
|----------------------|--------|--------|--------|--------|--------|-------|-------|--------|-------|--------|--------|-------|-------|
| Tm | 1.10 | 1.20 | 1.20 | 1.12 | 1.08 | 0.37 | 0.38 | 0.44 | 0.37 | 0.34 | 0.43 | 0.35 | 0.04 |
| Yb | 6.31 | 5.76 | 6.99 | 6.26 | 5.62 | 1.79 | 1.86 | 2.15 | 2.21 | 1.99 | 1.79 | 2.02 | 0.14 |
| Lu | 0.87 | 0.93 | 1.09 | 0.82 | 0.96 | 0.37 | 0.33 | 0.49 | 0.31 | 0.34 | 0.34 | 0.27 | 0.04 |
| LREE | 195.20 | 205.12 | 215.46 | 205.54 | 215.89 | 86.19 | 81.26 | 97.93 | 83.46 | 121.66 | 133.25 | 86.63 | 4.87 |
| HREE | 36.33 | 38.28 | 41.10 | 38.64 | 34.44 | 11.17 | 10.51 | 16.12 | 12.04 | 10.13 | 10.52 | 9.42 | 1.28 |
| LREE/HREE | 5.37 | 5.36 | 5.24 | 5.32 | 6.27 | 7.72 | 7.73 | 6.08 | 6.93 | 12.01 | 12.66 | 9.20 | 3.82 |
| ΣREE | 231.53 | 243.40 | 256.56 | 244.18 | 250.33 | 97.36 | 91.77 | 114.05 | 95.50 | 131.80 | 143.77 | 96.04 | 6.15 |
| δCe | 0.88 | 0.86 | 0.86 | 0.82 | 0.84 | 1.02 | 0.98 | 0.91 | 1.02 | 2.17 | 2.42 | 1.36 | 0.53 |
| δEu | 1.25 | 1.19 | 1.19 | 1.16 | 1.38 | 3.45 | 3.48 | 2.23 | 3.08 | 7.72 | 7.80 | 5.28 | 1.12 |
| (La/Yb) _N | 2.74 | 3.16 | 2.74 | 3.01 | 3.56 | 7.34 | 6.56 | 6.80 | 5.43 | 5.96 | 6.74 | 5.84 | 6.45 |
| (La/Sm) _N | 1.68 | 1.65 | 1.67 | 1.71 | 1.85 | 3.48 | 3.09 | 2.46 | 2.99 | 3.20 | 3.20 | 4.00 | 2.69 |
| (Gd/Yb) _N | 1.47 | 1.75 | 1.53 | 1.63 | 1.52 | 1.33 | 0.98 | 1.81 | 1.15 | 0.94 | 1.30 | 0.88 | 2.34 |
| Samples | MB-10 | MB-9 | MB-8 | MB-7 | MB-6 | MB-5 | MB-4 | MB-3 | MB-2 | MB-1 | MB-0 | TA-5 | TA-4 |
| La | 27.20 | 16.90 | 14.20 | 10.10 | 8.36 | 9.58 | 3.82 | 8.80 | 8.51 | 6.64 | 1.02 | 7.53 | 5.68 |
| Ce | 52.50 | 30.30 | 26.60 | 18.90 | 14.60 | 17.50 | 6.19 | 17.00 | 16.80 | 12.90 | 1.79 | 12.60 | 9.45 |
| Pr | 6.24 | 4.12 | 3.34 | 2.48 | 1.91 | 2.21 | 0.85 | 2.14 | 2.06 | 1.58 | 0.22 | 1.91 | 1.43 |
| Nd | 26.20 | 16.50 | 13.60 | 9.99 | 7.46 | 8.59 | 3.21 | 8.27 | 7.74 | 6.07 | 0.89 | 8.29 | 6.22 |
| Sm | 6.36 | 3.22 | 2.74 | 2.03 | 1.46 | 1.80 | 0.65 | 1.64 | 1.53 | 1.19 | 0.19 | 1.83 | 1.35 |
| Eu | 1.41 | 0.87 | 0.68 | 0.49 | 0.41 | 0.36 | 0.15 | 0.37 | 0.33 | 0.26 | 0.05 | 0.50 | 0.36 |
| Gd | 5.78 | 3.02 | 2.74 | 1.82 | 1.22 | 1.72 | 0.77 | 1.32 | 1.06 | 1.08 | 0.26 | 1.29 | 1.48 |
| Tb | 0.72 | 0.46 | 0.38 | 0.33 | 0.22 | 0.22 | 0.09 | 0.21 | 0.15 | 0.10 | 0.02 | 0.31 | 0.31 |
| Dy | 4.66 | 3.14 | 2.67 | 1.80 | 1.22 | 1.43 | 0.70 | 1.37 | 1.33 | 1.12 | 0.18 | 2.02 | 1.53 |
| Ho | 0.80 | 0.60 | 0.41 | 0.36 | 0.22 | 0.29 | 0.13 | 0.32 | 0.28 | 0.24 | 0.05 | 0.42 | 0.26 |
| Er | 2.39 | 1.66 | 1.26 | 0.95 | 0.76 | 0.69 | 0.32 | 0.67 | 0.72 | 0.61 | 0.08 | 1.09 | 0.84 |
| Tm | 0.45 | 0.35 | 0.33 | 0.21 | 0.15 | 0.16 | 0.06 | 0.16 | 0.12 | 0.11 | 0.01 | 0.34 | 0.20 |
| Yb | 2.83 | 2.12 | 1.82 | 1.14 | 0.70 | 0.72 | 0.44 | 0.80 | 0.72 | 0.85 | 0.11 | 1.32 | 0.65 |
| Lu | 0.45 | 0.27 | 0.18 | 0.20 | 0.14 | 0.11 | 0.09 | 0.15 | 0.18 | 0.08 | 0.01 | 0.14 | 0.18 |
| LREE | 119.91 | 71.91 | 61.16 | 43.99 | 34.20 | 40.04 | 14.86 | 38.22 | 36.97 | 28.64 | 4.16 | 32.66 | 24.49 |
| HREE | 18.07 | 11.61 | 9.80 | 6.81 | 4.62 | 5.32 | 2.60 | 5.00 | 4.58 | 4.19 | 0.73 | 6.93 | 5.44 |
| LREE/HREE | 6.63 | 6.19 | 6.24 | 6.46 | 7.40 | 7.52 | 5.72 | 7.65 | 8.07 | 6.84 | 5.74 | 4.71 | 4.50 |
| ΣREE | 137.98 | 83.52 | 70.96 | 50.80 | 38.82 | 45.36 | 17.45 | 43.22 | 41.55 | 32.82 | 4.89 | 39.59 | 29.93 |
| δCe | 0.97 | 0.87 | 0.93 | 0.91 | 0.88 | 0.92 | 0.83 | 0.94 | 0.97 | 0.96 | 0.91 | 0.80 | 0.80 |
| δEu | 2.41 | 2.70 | 2.70 | 2.73 | 3.04 | 2.77 | 2.44 | 3.21 | 3.67 | 3.16 | 2.20 | 2.28 | 1.86 |
| (La/Yb) _N | 6.48 | 5.37 | 5.26 | 5.97 | 8.03 | 9.03 | 5.88 | 7.45 | 7.96 | 5.28 | 6.43 | 3.85 | 5.86 |
| (La/Sm) _N | 2.69 | 3.30 | 3.26 | 3.13 | 3.60 | 3.35 | 3.72 | 3.38 | 3.50 | 3.51 | 3.31 | 2.59 | 2.65 |
| (Gd/Yb) _N | 1.65 | 1.15 | 1.21 | 1.29 | 1.40 | 1.94 | 1.42 | 1.34 | 1.19 | 1.03 | 1.99 | 0.79 | 1.83 |

Table 4. Cont.

| Samples | MC-0 | MC-1 | MC-2 | MC-3 | MC-4 | MC-5 | MC-6 | MC-7 | MC-8 | MC-9 | MC-10 | MC-11 | MC-12 |
|----------------------|-------|-------|-------|-------|-------|------|------|------|------|------|-------|-------|-------|
| Er | 1.51 | 1.66 | 1.25 | 1.85 | 1.30 | | | | | | | | |
| Tm | 0.35 | 0.38 | 0.27 | 0.34 | 0.17 | | | | | | | | |
| Yb | 2.38 | 2.45 | 1.44 | 2.19 | 1.20 | | | | | | | | |
| Lu | 0.25 | 0.45 | 0.36 | 0.32 | 0.27 | | | | | | | | |
| LREE | 10.48 | 12.85 | 11.86 | 10.34 | 7.74 | | | | | | | | |
| HREE | 10.24 | 10.78 | 8.04 | 9.94 | 7.20 | | | | | | | | |
| LREE/HREE | 1.02 | 1.19 | 1.47 | 1.04 | 1.08 | | | | | | | | |
| ΣREE | 20.72 | 23.63 | 19.90 | 20.27 | 14.94 | | | | | | | | |
| δCe | 0.21 | 0.16 | 0.25 | 0.26 | 0.26 | | | | | | | | |
| δEu | 0.20 | 0.19 | 0.34 | 0.26 | 0.24 | | | | | | | | |
| (La/Yb) _N | 0.75 | 0.98 | 1.45 | 0.74 | 1.01 | | | | | | | | |
| (La/Sm) _N | 1.26 | 1.49 | 1.52 | 1.09 | 1.10 | | | | | | | | |
| (Gd/Yb) _N | 0.77 | 0.73 | 0.87 | 0.64 | 1.12 | | | | | | | | |

All rare earth element values are in ppm; ΣREE = the sum of La to Lu, $\delta\text{Ce} = \text{Ce}_N / (\text{La}_N * \text{Pr}_N)^{0.5}$, $\delta\text{Eu} = \text{Ce}_N / (\text{Sm}_N * \text{Gd}_N)^{0.5}$, and La_N/Yb_N , La_N/Sm_N , Gd_N/Yb_N , where N refers to a chondrite-normalized value [46].

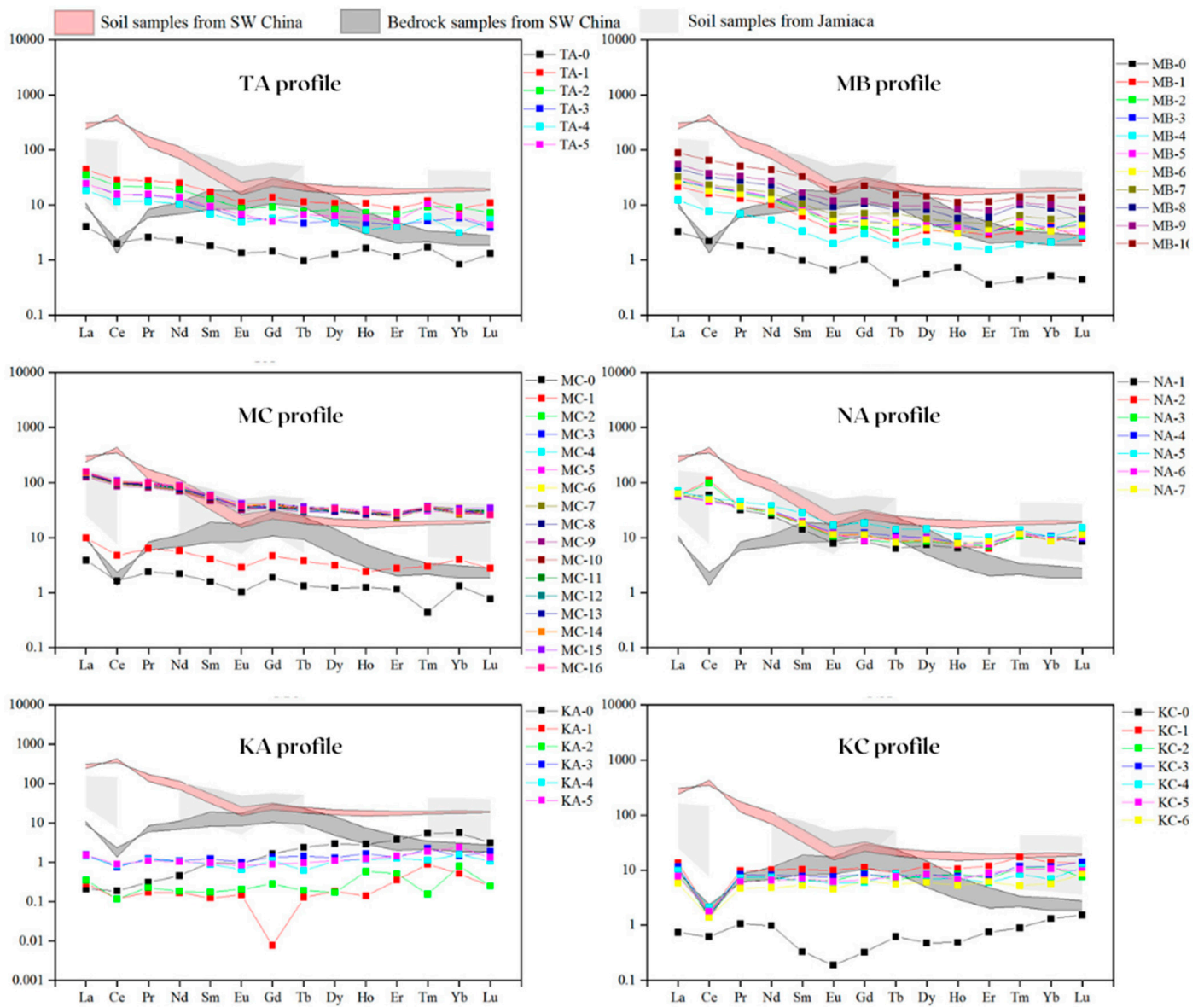


Figure 4. The REE chondrite-normalized patterns for six red soil profiles in two districts in Indonesia. Limestone-based profiles (TA-MB), dolomite-based profiles (MC-NA) and basalt-based profiles (KA-KC) were normalized to the concentration in [47]. Data compared to samples from southern China and Jamaica [4,22–24,27], respectively.

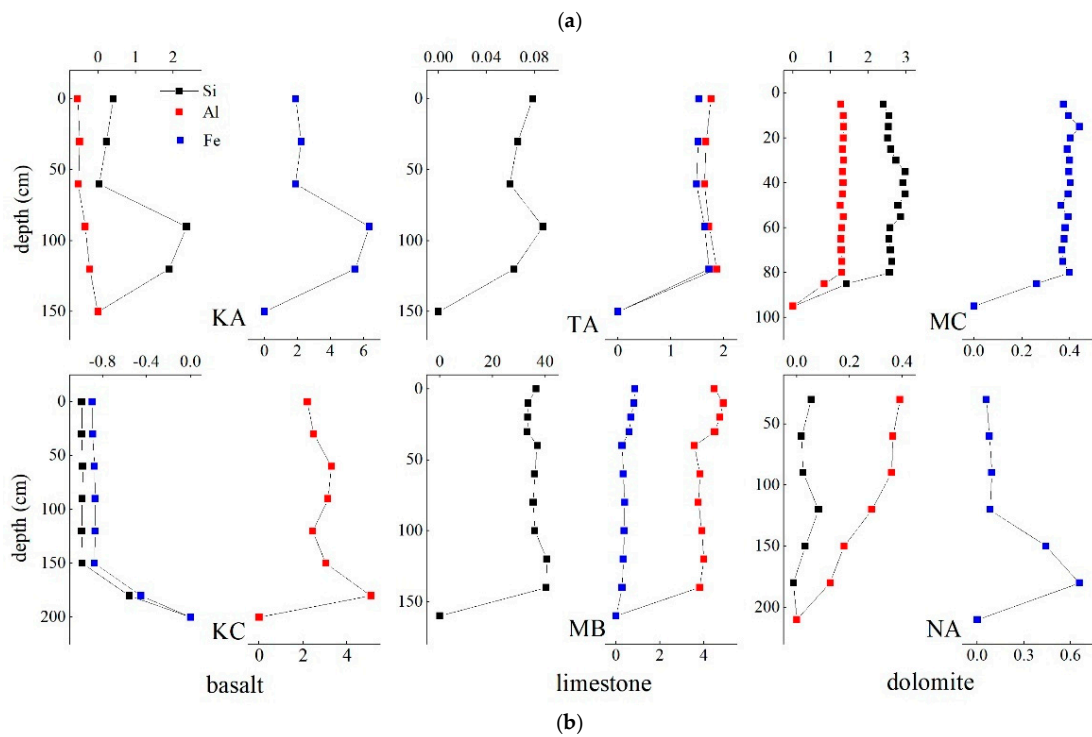


Figure 5. Major element migration coefficients ($\tau_{Th,j}$) vs. depth for six red soil profiles taken from the studied soil profiles in Indonesia. (a) Si, Al and Fe migration coefficients ($\tau_{Th,j}$) and (b) Mg, Ca, Na, K, Mn and P migration coefficients ($\tau_{Th,j}$).

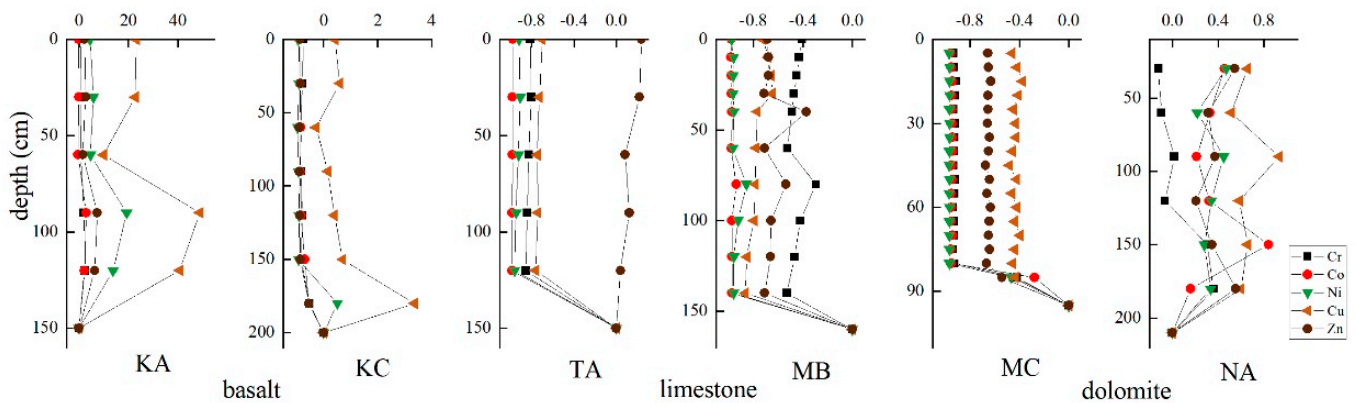


Figure 6. Transitional element migration coefficients ($\tau_{Th,j}$) vs. depth for six red soil profiles taken from the studied soil profiles in Indonesia.

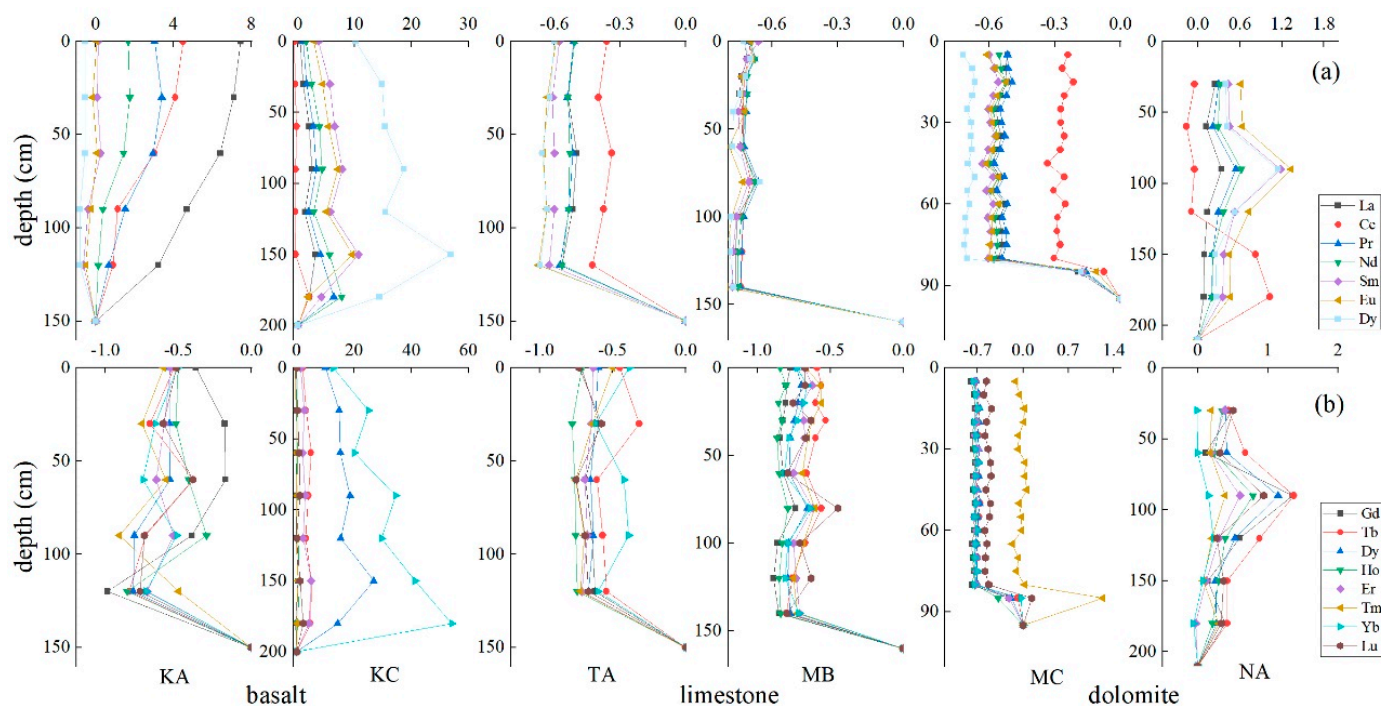


Figure 7. Rare earth element migration coefficients ($\tau_{Th,j}$) vs. depth for six red soil profiles taken from the studied soil profiles in Indonesia. (a) LREE migration coefficients ($\tau_{Th,j}$) and (b) HREE migration coefficients ($\tau_{Th,j}$).

4. Discussion

4.1. Source of Red Soil Materials

4.1.1. Major Elements Evidence

Combination of major element ratios can be used to trace material source effectively [23]. In this study, the strong positive correlation between TiO_2 , Fe_2O_3 and Al_2O_3 reflects a similar linear relationship between bedrock and subsoil samples except for KA and NA profiles, respectively (Figure 8a,b). The characteristic straight-line correlation is the dissolution line of carbonate rock and suggests that soil profiles undergo typical in situ weathering [48]. Our results suggest that while the carbonate profiles (TA-MB, MC) and KC profile indicated possible in situ weathering, profiles KA and NA indicated external material contribution. Furthermore, the correlation between TiO_2 , Fe_2O_3/Al_2O_3 for KA and NA soil profiles were linked to the acidic nature of the profiles. For example, the strong correlation between pH vs. Al_2O_3 and TiO_2 for KA ($R^2 = 0.95$; 0.78) and NA ($R^2 = 0.80$; 0.79) profiles, respectively, suggests that pH influenced element mobility.

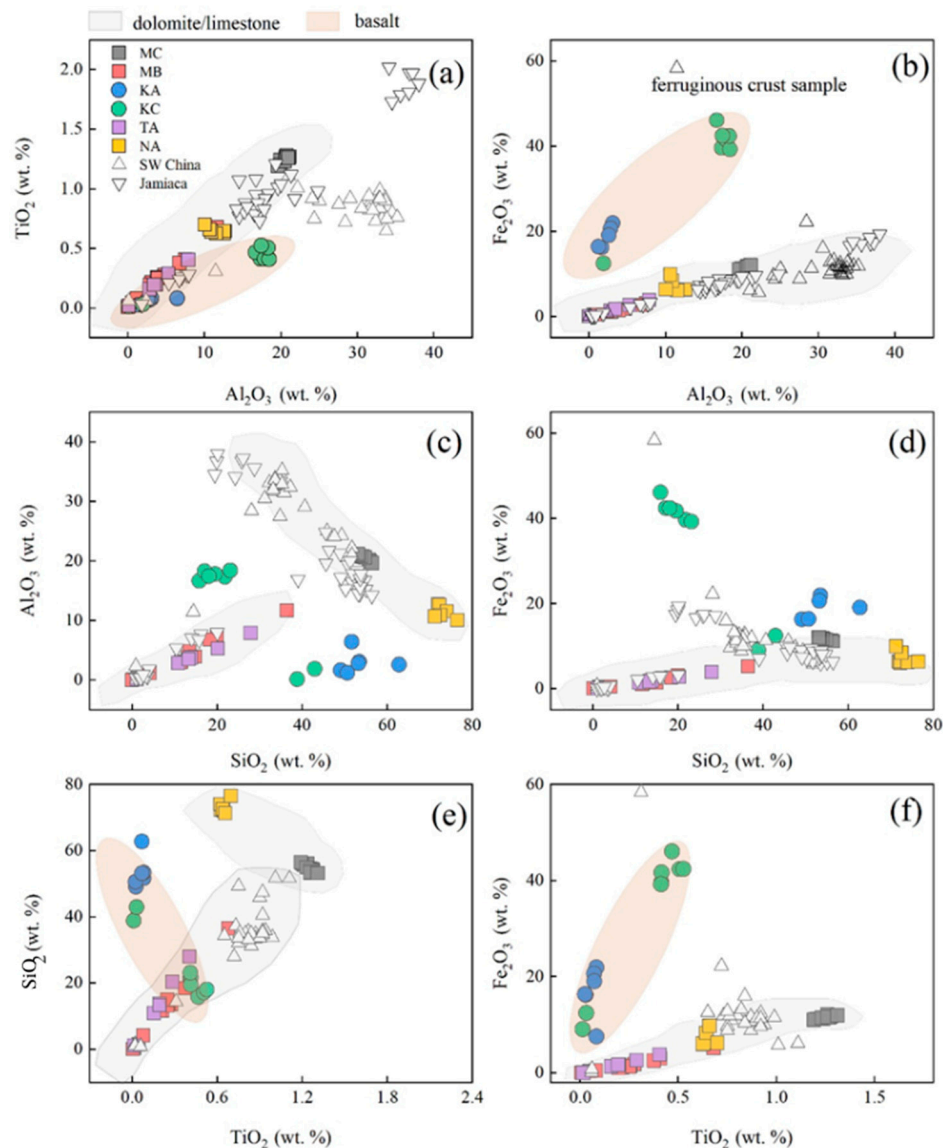


Figure 8. Distribution of major element oxides for six red soil profiles in two districts in Indonesia. (a) TiO₂ vs. Al₂O₃ (b) Fe₂O₃ vs. Al₂O₃ (c) Al₂O₃ vs. SiO₂ (d) Fe₂O₃ vs. SiO₂ (e) SiO₂ vs. TiO₂ (f) Fe₂O₃ vs. TiO₂. Data compared to samples from southern China and Jamaica [4,22–24,27], respectively.

4.1.2. Trace Element Evidence

Trace element distribution patterns can be used to trace the origin of weathering products [27]. The UCC normalized spider diagrams revealed similar trace element distribution patterns for the carbonate profiles (TA-MB; MC-NA) indicating inheritance and that the material has same provenance (Figure 3a,b,e,f); however, there was strong variation for the basalt profiles (Figure 3c,d). This was interpreted to be as a result of different sources or possible influence of external materials. The contribution of external material was later confirmed by the high field strength elements (HFSE) ratio, as these elements with different valence and ionic radii can be used to explain the addition of aeolian deposition during chemical weathering [34]. The binary plots in Figure 9 (a) Zr/Th, (b) Nb/Th, (c) Zr/TiO₂ and (d) TiO₂/Th indicate that the basalt profiles (KA-KC) and NA profiles may be influenced by aeolian deposition, while the straight-line fit confirms in situ weathering for the carbonate profiles (TA-MB and MC).

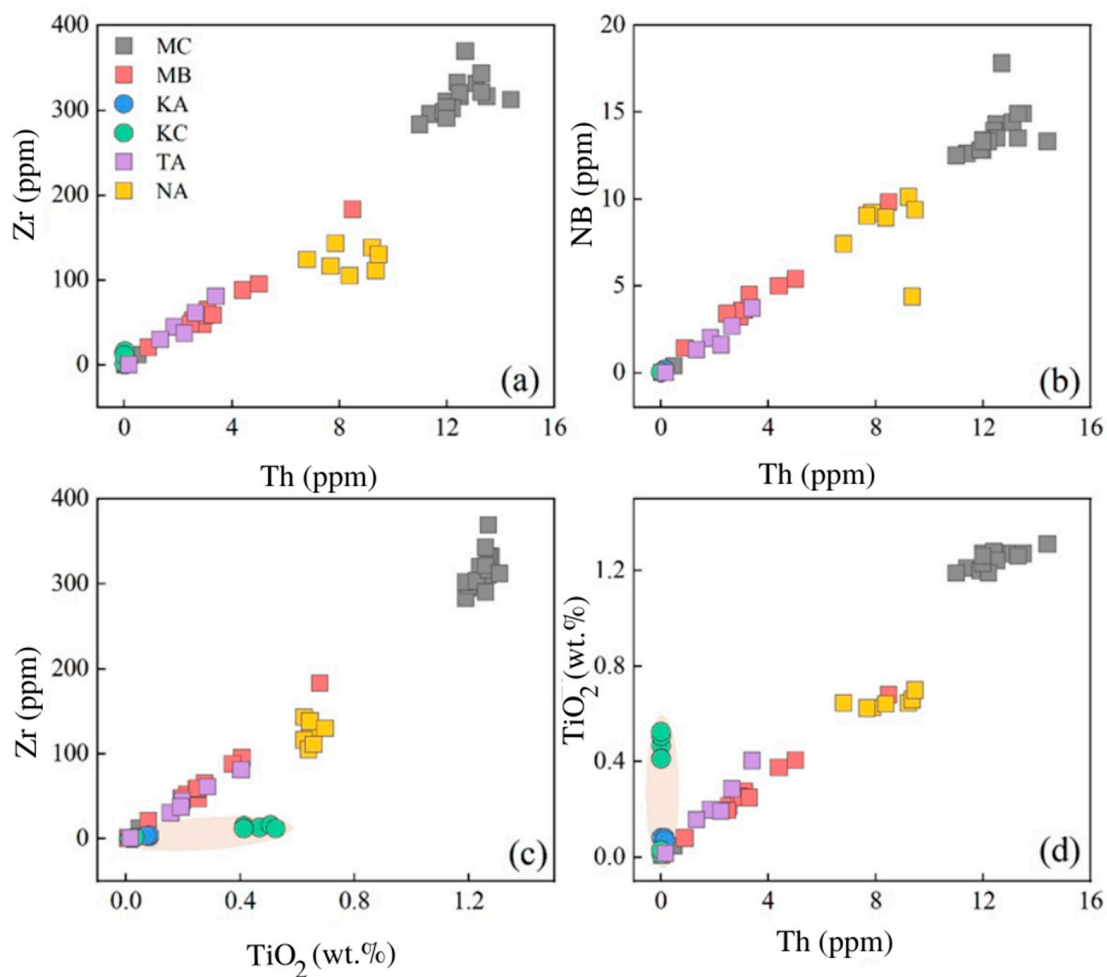


Figure 9. Binary plots of immobile elements (a) Zr/Th, (b) Nb/Th, (c) Zr/TiO₂ and (d) TiO₂/Th for six red soil profiles in two districts in Indonesia.

4.1.3. Rare Earth Elements Evidence

There is a typical REE pattern for rocks derived from upper continental crust [43] or from mixed sediments in the upper crust, such as loess [26,49]. For this study, the REE distribution pattern as displayed in the spider diagram indicated that the subsoil and bedrock of the carbonate profiles (TA-MB; MC-NA) have a similar pattern with an incline shape towards the right, suggesting clear inheritance (Figure 4). Conversely, the basalt profiles' (KA-KC) subsoil and bedrock samples are obviously different with no inclined trend, suggesting different sources [25] (Figure 4). The REE patterns were similar to those from southern China [22,27] and Jamaica [4] (Figure 4); however, they differ in Ce and Eu anomalies due to local physiochemical properties. Most of the soil profiles are relatively enriched in LREE, with negative Eu anomalies and relatively flat HREE curves. This REE pattern is typical of sediments derived from UCC and loess. Furthermore, rare earth element ratios (La_N/Yb_N and Gd_N/Yb_N) along with δEu parameters can reflect the evolution trend and source of sediments [24,50]. Post-Archean sedimentary rocks usually have REE composition values of $La_N/Yb_N < 15$ [43] while Chinese and Alaskan loesses have values ranging from 7–10 [26]. The scatter plot of δEu vs. La_N/Yb_N (Figure 10a) revealed that the red soil profiles' Eu values ranged from 0.06 in the KA profile to 10.11 in the KC profile. The δEu values of the carbonate profiles (TA-MB; MC-NA) were significantly larger than those of the basalt profiles (KA-KC) except for two samples of the MC profile (Figure 10a). The small δEu vs. La_N/Yb_N value range for KA-KC soil profiles recorded in this study is similar to those reported in Wei et al. for the basalt profile [27]. All our

samples were notably outside the UCC, Chinese loess and Emeishan basalt value range, except for the KC bedrock sample, which fell in the Emeishan basalt range. The potential source of Indonesia red soils was different when compared to southern China and Jamaica samples, which were within or in close proximity to African dust, Chinese loess and UCC value ranges (Figure 10a). Conversely, the δEu vs. $\text{Gd}_\text{N}/\text{Yb}_\text{N}$ plot for the red soil profiles showed the clustering of profiles in close proximity to the average UCC and Emeishan basalt values (Figure 10b). However, KA-KC soil profiles had the lowest values except for the two points in the KC soil profile. This result suggested that the basalt profiles (KA-KC) with a narrow δEu can be distinguished from the carbonate profiles (TA-MB; MC-NA), which have a wider range. In addition, the results clearly indicate some amount of mixing of source material and the influence of external material, especially for KC and NA profiles. According to the geochemical ratios discussed, the evidence strongly supports in situ weathering for carbonate profiles (TA-MB and MC), indicating a similar material source, i.e., limestone and dolomite, respectively. Conversely, the basalt profiles (KA-KC) and NA profile, although influenced by underlying bedrock, also had contribution from an external source. Our study further revealed some clustering of profiles with few sample points falling outside the average range of UCC, Chinese loess and Emeishan basalt values, representing potential detrital components, eolian material and igneous rocks, respectively (Figure 10a,b). The geochemical evidence supports the notion of mixing of material and the contribution of external materials. The profiles are located in a volcanic area surrounded by a complexity of other lithologies that can influence elemental composition and behavior.

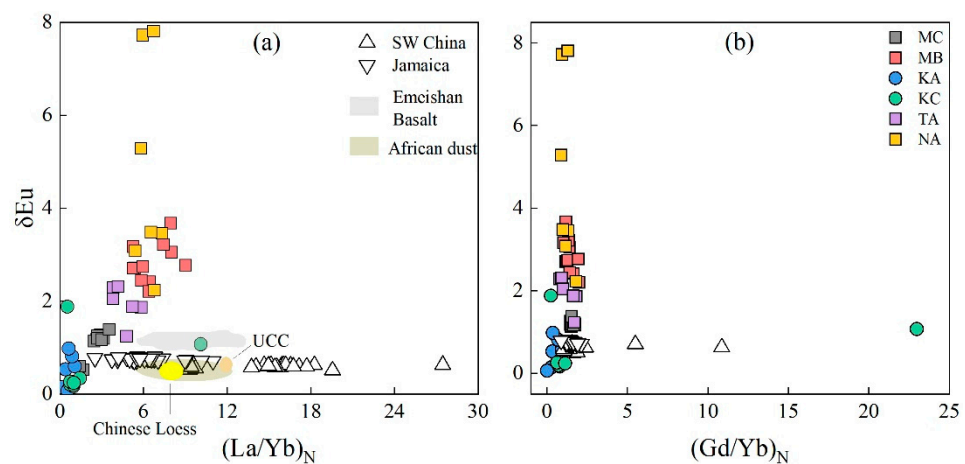


Figure 10. (a) δEu vs. $\text{La}_\text{N}/\text{Yb}_\text{N}$ and (b) δEu vs. $\text{Gd}_\text{N}/\text{Yb}_\text{N}$ plots for six red soil profiles in two districts in Indonesia compared with UCC, Chinese loess and Emeishan basalt for potential genesis.

4.2. Elemental Behavior during Weathering and Pedogenesis

Lateritic soil formation processes are mainly controlled by Fe, Al and Si geochemistry. The major element contents indicate positive correlations in the carbonate profiles, with few exceptions for the NA profile, which are similar to findings in southern China and Jamaica (Figure 8a–f). However, the basalt profiles indicate more variability with positive and negative correlations among the major elements (Figure 8a–f). The positive and negative correlations among these elements illustrate the accumulation and dissolution of mineral phases [23]. Major elements' behavior (Al, Fe) is primarily controlled by pH and redox and soil hydrological conditions due to the monsoon climate [23,24]. For example, the strong correlation between pH vs. Al for KC ($R^2 = 0.95$) and NA ($R^2 = 0.80$) soil profiles indicates that solubility of the element oxides is controlled by pH. Similarly, the acidic nature and water availability of KA-KC and NA profiles (low pH 4.6–5.5; Table 2) provided the reducing condition for the precipitation of Fe^{2+} -forming minerals. Lithology seems to have an influence on major elements' distribution and behavior, as the carbonate profiles indicate relatively even distribution and similar behavior while the basalt profiles and NA profile tend to indicate uneven distribution and show different behaviors among the major

elements. In the tropical humid climates, strong hydrolysis results in the rapid dissolution of weatherable minerals, e.g., plagioclase and pyroxene can be indicated by the loss of K, Na and Mg, respectively [51], and the formation of new secondary clay minerals and ferric hydrates. The consistently flat and elevated tau values for the carbonate profiles were because carbonate is much easier to dissolve, and therefore the originally small amounts of silicates in the carbonate rock are greatly inflated. In addition, the frequent wet–dry cycles and leaching activities result in the formation of different secondary clay minerals. The NA profile behaves differently due to its geomorphic position, being located between carbonate sedimentary rocks and unconsolidated sediments at much lower elevation and so being affected by eluviation and deposition of materials from other sources.

In our red soil profiles, some trace elements, such as Be, Rb and Sr concentrations in the subsoil samples of both carbonate and basalt profiles, were distinctly lower than UCC normalized spider values, i.e., <1 (Figure 3a–f). This indicates that these soluble mobile elements were strongly leached and exported from the soil profiles in solution after intense chemical weathering. Alkali elements K and Rb are dominant in K-feldspars, illite and kaolinite mineral [52], and they have similar chemical characteristics that may function similarly in minerals [53]. Meanwhile, the element Be can form complex hydroxides in solution, therefore can be leached from the profiles. The ionic potential of Sr^{2+} (1.8) is relatively similar to that of Ca^{2+} (2.0) [54] and so behaves chemically similar, hence is readily substituted as Ca in calcium carbonate [52]. As compared with the normalized UCC values, Sr is significantly depleted as rapid removal occurs during chemical weathering [38]. Similarly, heavy depletion of Rb and Sr were reported for limestone [22], dolomite [22,23] and basalt [27] in southern China.

According to the migration coefficient, the transitional elements Cr, Co, Ni, Cu and Zn are being constantly depleted throughout the carbonate profiles with no evidence of reconcentration at lower sections, except for the NA profile (Figure 6). Conversely, the enrichment in Cu, Ni and Zn in the basalt soil profiles may be due to the formation and precipitation of secondary mineral containing Fe, P and Mn oxide/hydroxides as there were strong correlations among the elements. Usually in a stable soil environment, some minerals tend to dissolve and to lose elements, whereas other minerals precipitate at lower sections to gain elements [35]. This oscillatory depletion and enrichment trend for $\tau_{\text{Th, j}}$ was not observed, which suggests that the dissolution and precipitation processes were not in equilibrium. The high Cr and Ni concentrations indicate the presence of a mafic component in the source region for KA-KC profiles. Furthermore, Fu et al. [30] pointed out that besides olivine, primary serpentine may provide an extra source of Ni in laterite soils. The behavior of multiple valence elements, e.g., Co, Cr, is considered to be redox-sensitive during chemical weathering [55–59]. The element Co naturally occurs as Co^{2+} in solutions whereas the solubility of Co^{3+} is extremely low [55]. Similarly, the reduced Cr^{3+} ions are immobile and insoluble [60]; however, under oxidized condition Cr forms soluble oxygen-bearing compounds, and transports as chromate or dichromate [60–62].

Generally, under mild and humid conditions, intense chemical weathering allows REEs to become more mobile [27]. The REE contents in the KA profile (Figure 4) were relatively low, which we interpreted as a low proportion of REE-bearing minerals such as allanite, monazite, xenotime and apatite [63]. The constant depletion in REEs (LREE and HREE) throughout the entire carbonate profiles, as indicated by the migration coefficient, was attributed to the dissolution of stable REE-bearing minerals [64] as a result of the monsoonal climate. However, the enrichment in LREE for the basalt (KA-KC) and NA profiles was due to the ability of the ions to form stable secondary minerals, resulting in accumulation at different sections of the profiles (Figure 7a). This was confirmed by the positive correlation between REEs and Cr, Co, Fe, P and Mn. The enrichment of LREEs is mostly common in the supergene environment as stated by Braun et al. [65], indicating that LREEs are more distributed in laterite profiles. The enrichment in LREEs has been inherited from the parent rock and may be due to the formation of secondary LREE-bearing minerals such as rhabdophane [63]. The mobilization or fractionation of REEs in weathering profiles

is mainly controlled by weathering conditions and the stability of primary and secondary REE-bearing minerals [63,66]. Similarly, the relatively stable HREEs in the KA profile was entirely leached and transported out of the profile by soil solutions after extreme weathering. REEs' fractionation occurs during late stages of chemical weathering. The fractionation is caused by the preferential leaching of rocks comprised of stable and unstable minerals, hence the uneven distribution of elements in the basalt and NA profiles while the carbonate profiles were composed of stable minerals containing REEs. A similar REE distribution and behavior pattern was reported for carbonate soil samples from southern China [22,27] and Jamaica [4] with the exception in Ce and Eu anomalies; however, it was slightly different for basalt profiles, especially the KA profile (Figure 4). Most stable REEs have an oxidation state of 3+ [67]; Ce and Eu are quite different as they may occur in a 2+ reducing state and 4+ oxidizing state [55]. During chemical weathering, Ce^{3+} is readily oxidized to Ce^{4+} and precipitate as CeO_2 [61,65,68]. Therefore, the increase in Ce for the NA profile resulted from oxidizing conditions present in the lower section. A similar increase in Ce was reported for soil samples from southern China (Figure 4). On the other hand, the depletion in Ce for the carbonate bedrock samples was similar to findings reported by Ji et al. [24], which suggested that carbonate weathering crust usually exhibited a negative Ce abnormality. Most carbonate bedrocks display a negative Ce anomaly due to ionic radii and coordination numbers [67]. The behavior of Ce in KA and KC profiles was due to the acidic conditions as there was correlation with pH ($R^2 = 0.46, 0.86$), respectively. Similarly, the Eu^{2+} ionic radii behavior was influenced by redox reactions. The ionic radii of Eu^{2+} closely resembles that of Sr^{2+} and so they display similar geochemical behavior under reducing conditions [69]. The negative Eu anomalies indicate that Eu-bearing phase minerals are being preferentially dissolved during weathering, which is consistent with the dissolution of plagioclase in lithologies [70]. The negative Eu anomaly display by the limestone and dolomite profiles may be linked to the partial dissolution of feldspars [55]. Based on the normalized spider diagrams, migration coefficient and the geochemical tracer evidence discussed, the red soils in Indonesia experienced dynamic elemental behavior. The accumulation and depletion of preferential trace and REEs in the soil profiles were due to the nature of the parent rock, controlled by the stability of secondary oxides/hydroxides and redox sensitivity of the environment.

4.3. Chemical Weathering and Pedogenesis of Red Soil Profiles

Chemical weathering and pedogenesis processes represent the dissolution of plagioclase/feldspar and illite/smectite minerals and the formation of gibbsite and kaolinite minerals [23]. Under strong leaching and acidic conditions, feldspar intensely weathers and hydrolyses, and kaolinite can be mass produced by neoformation [71]. The ternary diagram (A-CN-K) indicates the molar proportions of Al_2O_3 , (A-apex), $CaO + NaO$ (CN-apex) and K_2O (K-apex); these are commonly used to illustrate weathering intensity and trend [72]. According to the ternary diagram in this study, most of the soil samples indicate intense chemical weathering conditions (Figure 11a,b) with subsoil samples clumped at the A apex. The basalt profiles (KA-KC) and MC profile are found at the extreme tip of the apex, followed by TA soil samples which fall left, along the A-CN join to Al_2O_3 apex. Conversely, the NA and MB profiles fall to the right along the A-K join to the Al_2O_3 apex, indicating the depletion of K_2O , CaO and Na_2O and enrichment of Al_2O_3 during the formation of secondary clay minerals. This weathering trend towards the production of gibbsite and kaolinite minerals is often seen in subtropical and tropical regions [73]. The position of the KA-KC and MC profiles on the diagram were supported by high average CIA values of 97, 99.4 and 98.9, respectively, although some soil samples generally overlap. Similar findings were reported by Ji et al. [23,24,74] and Lu et al. [75] whereby the bulk of the soil samples accumulated in the A apex region. The clay mineral was dominated by kaolinite and gibbsite followed by few samples with minerals illite and smectite. The small variation in clay mineral assemblages and weathering degree may be attributed to the difference in lithology and age. The intrusive rocks and metamorphic rocks from the region are much

older and exposed to the surface longer than sedimentary rocks, as reported by Peucker-Ehrenbrink and Miller [76]. Furthermore, chemical weathering seems to be more advanced in the basalt profiles (KA-KC) than in the carbonate profiles. During the initial stage of weathering, particularly at the weathering front, the basalt bedrock samples (KA-KC) have higher CIA values of 85 and 72, respectively, indicating moderate weathering intensity, while the carbonate bedrocks have much lower CIA values (18–61). Mafic minerals such as pyroxenes or chlorite generally weathered more readily than quartz or orthoclase [77]. In addition, elevation could also explain the small variation in clay mineral assemblages and weathering degree, as the lower elevation profiles tend to have higher CIA values. Similarly, Ouyang et al. [78] pointed out that clay mineral composition is related to the parent material, climate and micro-topography. Chemical weathering intensity in red soil profiles can be estimated by the CIA [18]. Generally, a CIA values range of 60–80 indicates moderate weathering degree, while values in the range of 80–100 indicate intense weathering [79–81]. The red soils in Indonesia recorded high CIA values, especially in the subsoil layer, with an average value of >92 indicating intense chemical weathering (Table 2). This represents a shift from illite/smectite to gibbsite/kaolinite in these profiles, as CIA increases towards 100 (Figure 11a,b). Kaolinite is the most stable phyllosilicate mineral in extreme hydrolytic weathering environments and therefore the dominant secondary mineral in highly weathered soils [82]. In comparison to other CIA values, our values are slightly similar to those reported in Ji et al., Wei et al., Lu et al. and Beckford et al. [23,27,75,83] for southern China, but higher than those reported for UCC [42], NASC [84], European red clay [85,86], the world-wide loess [49] and the red earth of eastern China [80]. This finding suggests that red soils are strongly weathered and may be distributed along geographical latitude with similar climate, where the prevailing environmental conditions have remained constant over a long geological time. The relationship between CIA and the major oxides (Figure 12a–f) revealed mostly a positive correlation for the carbonate profiles, except, however, for a few oxides in the basalt profiles (KA-KC) and NA profile. In contrast, the content of CaO indicates a negative correlation with CIA for all the red soil profiles, which was similar to findings reported by Wei et al. [27] for southern China. The general negative relationship between CIA values and CaO indicates that the variation is linked to the weathering intensity of the soils. The negative correlation of CIA with TiO_2 , Fe_2O_3 and SiO_2 contents in KA-KC and NA profiles cannot be explained as control of quartz on CIA, but rather by the influence of pH.

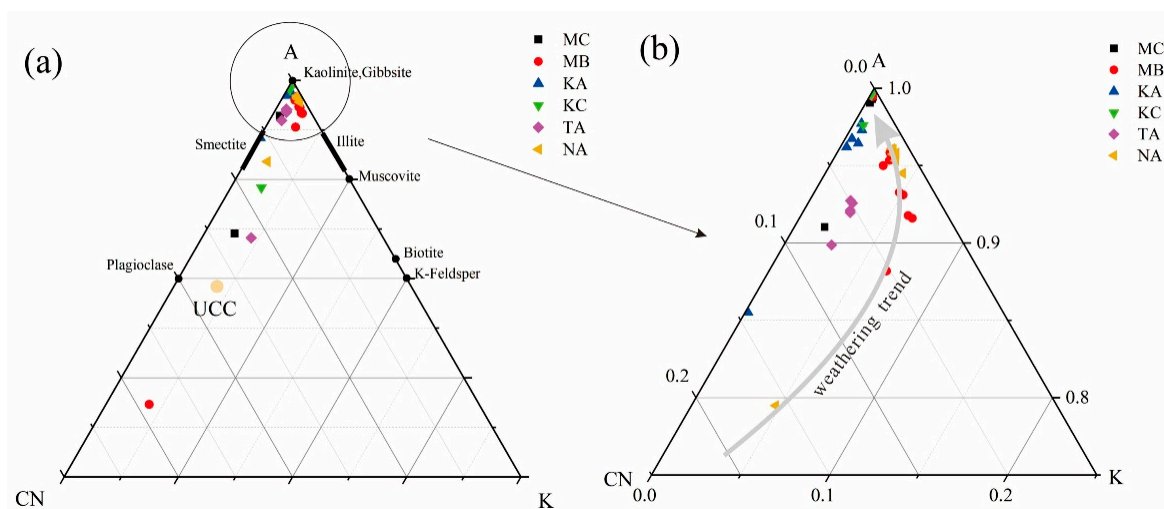


Figure 11. (a) Basic A-CN-K ternary diagram for six red soil profiles in two districts in Indonesia where $Al_2O_3 = (A)$, $CaO+Na_2O = (CN)$ and $K_2O = (K)$. The position and orientation of minerals is in accordance with [72]. (b) Magnified apex region showing weathering trend [72].

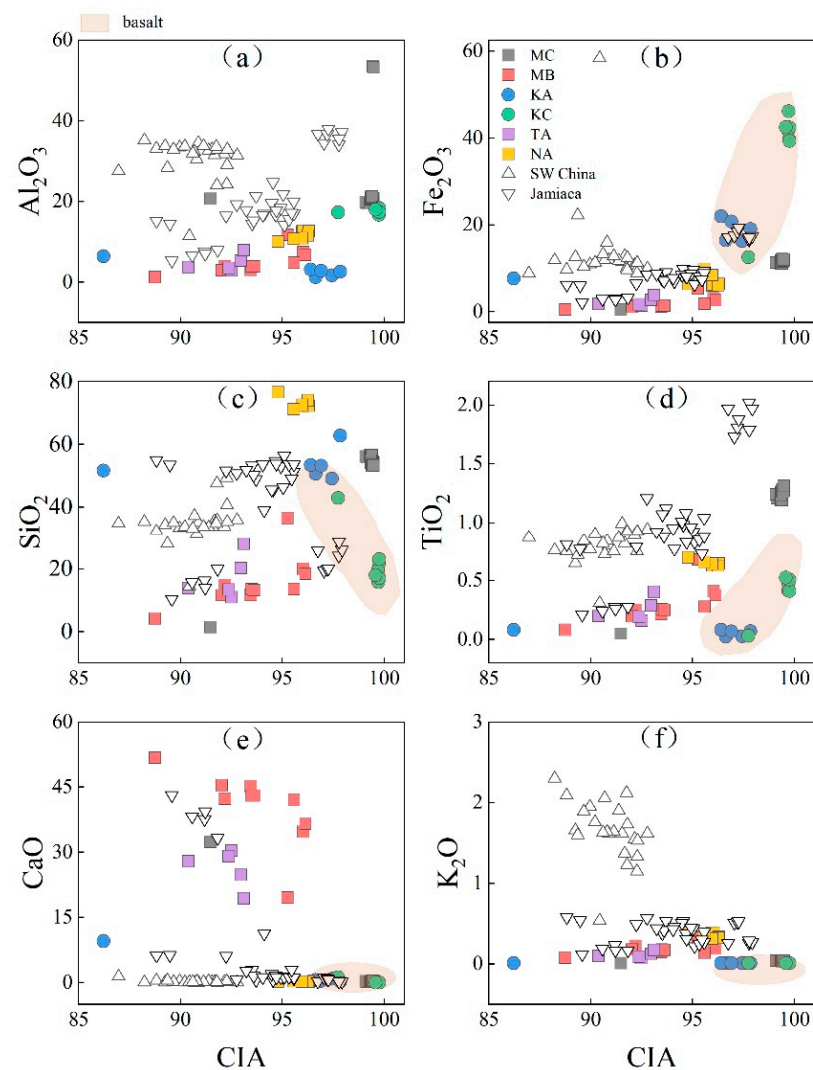


Figure 12. Variation plots of major oxides versus CIA for the six red soil profiles in two districts in Indonesia. (a) Al_2O_3 , (b) Fe_2O_3 , (c) SiO_2 , (d) TiO_2 , (e) CaO , (f) K_2O vs. CIA. Data compared to samples from southern China and Jamaica [4,22–24,27], respectively.

5. Conclusions

Our findings from the geochemical evidence materialized in this research indicate that red soils from carbonate profiles have similar material sources with close inheritance to that of the underlying bedrock. The basalt profiles, while having close affinity to their bedrock, also show an external material contribution. Furthermore, the weak correlations of immobile element ratios Zr/Th , Nb/Th , Zr/Ti and Ti/Th for the basalt profiles and NA profile confirmed external material contribution. In comparison to the average UCC, Chinese loess and Emeishan basalt samples, the end members in this study indicate mixing and some amount of foreign material contribution. The geochemical evidence and elemental ratio suggest that the red soils of Indonesia more likely originate from a combination of insoluble residues of parent bedrock and polygenetic sources. The carbonate profiles were characterized by having enrichment in major elements (Al, Fe, Si) with preferential depletion in bases (K, Na) while the basalt profiles experienced both enrichment and depletion among the elements. In addition, the other elemental group (transitional and rare earth elements) revealed dynamic behavior with relatively constant depletion and even distribution throughout the carbonate profiles, while the basalt profiles indicate uneven distribution with enrichment and depletion in different sections of the profiles. The variation in elemental behavior and weathering intensity are linked to lithologies, age and local

physiochemical conditions. The dynamic elemental behavior and high weathering degree have important implications, not only for the origin and evolution of red soils in tropical areas, but also for the role they play in the global element cycle.

Author Contributions: Conceptualization, H.O.B.; methodology, H.J.; formal analysis, H.O.B.; funding acquisition, H.J.; resources, H.J.; writing—original draft, H.O.B.; writing—review and editing, C.C., H.J. and H.O.B.; supervision, H.J. All authors have read and agreed to the published version of the manuscript.

Funding: This research was funded by the National Natural Science Foundation of China (NSFC) grants (41473122, 41073096), the National Key Basic Research Program of China (2013CB956702) and the Hundred Talents Program of the Chinese Academy of Sciences.

Data Availability Statement: The data are available on request from the corresponding author.

Acknowledgments: The authors acknowledge any support given not covered by the author contribution or funding sections. This includes administrative and technical support, and donations in kind (e.g., materials used for experiments).

Conflicts of Interest: The authors declare no conflict of interest.

References

- Birkeland, P.W. *Soils and Geomorphology*; Oxford University Press: London, UK, 1999.
- Mee, A.C.; Bestland, E.A.; Spooner, N.A. Age and origin of Terra Rossa soils in the Coonawarra area of South Australia. *Geomorphology* **2004**, *58*, 1–25. [[CrossRef](#)]
- Muhs, D.R.; Bettis, E.A.; Been, J.; Mcgeehin, J.P. Impact of Climate and Parent Material on Chemical Weathering in Loess-derived Soils of the Mississippi River Valley. *Soil Sci. Soc. Am. J.* **2001**, *65*, 1761–1777. [[CrossRef](#)]
- Muhs, D.R.; Budahn, J.R. Geochemical evidence for African dust and volcanic ash inputs to terra rossa soils on carbonate reef terraces, northern Jamaica, West Indies. *Quat. Int.* **2009**, *196*, 13–35. [[CrossRef](#)]
- Olson, C.G.; Ruhe, R.V.; Mausbach, M.J. The terra rossa limestone contact phenomena in karst, Southern Indiana. *Soil Sci. Soc. Am. J.* **1980**, *44*, 1075–1079. [[CrossRef](#)]
- Wiharso, D. Characteristics of Red Soils from The University of Lampung Experiment Station in Tanjung, South Lampung. *J. Trop. Soil* **1996**, *2*, 15–22.
- FAO. *World Reference Base for Soil Resources. International Soil Classification System for Naming Soils and Creating Legends for Soil Maps*; Update 2015; World Soil Resources Report No. 106; FAO: Rome, Italy, 2015.
- Feng, J.L.; Cui, Z.J.; Zhu, L.P. Origin of terra rossa over dolomite on the Yunnan Guizhou Plateau, China. *Geochem. J.* **2009**, *43*, 151–166. [[CrossRef](#)]
- Sustersic, F.; Rejsek, K.; Misic, M.; Eichler, F. The role of loamy sediment in the context of steady state karst surface lowering. *Geomorphology* **2009**, *106*, 35–45. [[CrossRef](#)]
- Merino, E.; Banerjee, A. Terra rossa genesis, implications for karst, and eolian dust; a geodynamic thread. *J. Geol.* **2008**, *116*, 62–75. [[CrossRef](#)]
- Berner, R.A.; Lasaga, A.C.; Garrels, R.M. The carbonate–silicate geochemical cycle and its effect on atmospheric carbon-dioxide over the past 100 million years. *Am. J. Sci.* **1983**, *283*, 641–683. [[CrossRef](#)]
- Berner, R.A.; Berner, E.K. Silicate weathering and climate. In *Tectonic Uplift and Climate Change*; Springer: New York, NY, USA, 1997; pp. 19–40.
- Dessert, C.; Dupré, B.; Gaillardet, J.; François, L.M.; Allègre, C.J. Basalt weathering laws and the impact of basalt weathering on the global carbon cycle. *Chem. Geol.* **2003**, *202*, 257–273. [[CrossRef](#)]
- Gislason, S.R.; Oelkers, E.H.; Eiriksdottir, E.S.; Kardjilov, M.I.; Gisladottir, G.; Sigfusson, B.; Snorrason, A.; Elefsen, S.; Hardardottir, J.; Torssander, P.; et al. Direct evidence of the feedback between climate and weathering. *Earth Planet. Sci. Lett.* **2009**, *277*, 213–222. [[CrossRef](#)]
- Jha, P.K.; Tiwari, J.; Singh, U.K.; Kumar, M.; Subramanian, V. Chemical weathering and associated CO₂ consumption in the Godavari River basin, India. *Chem. Geol.* **2009**, *264*, 364–374. [[CrossRef](#)]
- Kump, L.R.; Brantley, S.L.; Arthur, M.A. Chemical, weathering, atmospheric CO₂, and climate. *Annu. Rev. Earth Planet. Sci.* **2000**, *28*, 611–667. [[CrossRef](#)]
- Lerman, A.; Wu, L.L.; Mackenzie, F.T. CO₂ and H₂SO₄ consumption in weathering and material transport to the ocean, and their role in the global carbon balance. *Mar. Chem.* **2007**, *106*, 326–350. [[CrossRef](#)]
- Nesbitt, H.W.; Young, G.M. Early Proterozoic climates and plate motions inferred from major element chemistry of lutites. *Nature* **1982**, *229*, 715–717. [[CrossRef](#)]
- Scott, C.; Lyons, T.W.; Bekker, A.; Shen, Y.; Poulton, S.W.; Chu, X.; Anbar, A.D. Tracing the stepwise oxygenation of the Proterozoic Ocean. *Nature* **2008**, *452*, 456–459. [[CrossRef](#)]

20. Wang, L.; Zhang, L.J.; Cai, W.J.; Wang, B.S.; Yu, Z.G. Consumption of atmospheric CO₂ via chemical weathering in the Yellow River basin: The Qinghai-Tibet Plateau is the main contributor to the high dissolved inorganic carbon in the Yellow River. *Chem. Geol.* **2016**, *430*, 34–44. [[CrossRef](#)]
21. White, A.F.; Brantley, S.L. Chemical weathering rates of silicate minerals: An overview. In: *Chemical Weathering. Rates of Silicate Minerals* **1995**, *31*, 1–22.
22. Cao, X.; Wu, P.; Cao, Z. Element geochemical characteristics of a soil developed on dolomite in central Guizhou, southern China: Implications for parent materials. *Acta Geochem.* **2016**, *35*, 445–462. [[CrossRef](#)]
23. Ji, H.B.; Wang, S.J.; Ouyang, Z.Y.; Zhang, S.; Sun, C.X.; Liu, X.M.; Zhou, D.Q. Geochemistry of red residua underlying dolomites in karst terrains of Yunnan–Guizhou Plateau: I. The formation of the Pingba profile. *Chem. Geol.* **2004**, *203*, 1–27. [[CrossRef](#)]
24. Ji, H.B.; Wang, S.J.; Ouyang, Z.Y.; Zhang, S.; Sun, C.X.; Liu, X.M.; Zhou, D.Q. Geochemistry of red residua underlying dolomites in karst terrains of Yunnan–Guizhou Plateau: II. The mobility of rare earth elements during weathering. *Chem. Geol.* **2004**, *203*, 29–50. [[CrossRef](#)]
25. Jiang, K.; Hua-Wen, Q.; Rui-Zhong, H. Element mobilization and redistribution under extreme tropical weathering of basalts from the Hainan Island, South China. *J. Asian Earth Sci.* **2018**, *158*, 80–102. [[CrossRef](#)]
26. Muhs, D.R.; Budahn, J.R. Geochemical evidence for the origin of late Quaternary loess in central Alaska. *Can. J. Earth Sci.* **2006**, *43*, 323–337. [[CrossRef](#)]
27. Wei, X.; Ji, H.B.; Li, D.; Zang, F.; Wang, S.J. Material source analysis and element geochemical research about two types of representative bauxite deposits and terra rossa in western Guangxi, southern China. *J. Geochem. Explor.* **2013**, *133*, 68–87. [[CrossRef](#)]
28. Aldrian, E.; Dwi Susanto, R. Identification of Three Dominant Rainfall Regions within Indonesia and Their Relationship to Sea Surface Temperature. *Int. J. Climatol.* **2003**, *23*, 1435–1452. [[CrossRef](#)]
29. Li, X.Y.; Zhang, Z.W.; Wu, C.Q.; Xu, J.H.; Jin, Z.R. Geology and geochemistry of Gunung Subang gold deposit, Tanggeung, Cianjur, West Java, Indonesia. *Ore Geol. Rev.* **2019**, *113*, 103060. [[CrossRef](#)]
30. Fu, W.; Yang, J.; Yang, M.; Pang, B.; Liu, X.; Niu, H.; Huang, X. Mineralogical and geochemical characteristics of a serpentinite-derived laterite profile from East Sulawesi, Indonesia: Implications for the lateritization process and Ni supergene enrichment in the tropical rainforest. *J. Asian Earth Sci.* **2014**, *93*, 74–88. [[CrossRef](#)]
31. Wang, M.; Nan, C.; Wang, Z. *Determination of pH in Soil*; China Agriculture Press: Beijing, China, 2007.
32. Soil Survey Staff. *Keys to Soil Taxonomy*, 12th ed.; USDA—Natural Resources Conservation Service: Washington, DC, USA, 2014.
33. Babechuk, M.G.; Widdowson, M.; Kamber, B.S. Quantifying chemical weathering intensity and trace element release from two contrasting basalt profiles, Deccan Traps, India. *Chem. Geol.* **2014**, *363*, 56–75. [[CrossRef](#)]
34. Babechuk, M.G.; Widdowson, M.; Murphy, M.; Kamber, B.S. A combined Y/Ho, high field strength element (HFSE) and Nd isotope perspective on basalt weathering, Deccan Traps, India. *Chem. Geol.* **2015**, *396*, 25–41. [[CrossRef](#)]
35. Brantley, S.L.; Lebedeva, M. Learning to read the chemistry of regolith to understand the Critical Zone. *Annu. Rev. Earth Planet. Sci.* **2011**, *39*, 387–416. [[CrossRef](#)]
36. Kurtz, A.C.; Derry, L.A.; Chadwick, O.A.; Alfano, M.J. Refractory element mobility in volcanic soils. *Geology* **2000**, *28*, 683–686. [[CrossRef](#)]
37. Nesbitt, H.W. Mobility and fractionation of Rare-Earth elements during weathering of a granodiorite. *Nature* **1979**, *279*, 206–210. [[CrossRef](#)]
38. Nesbitt, H.W.; Markovics, G.; Price, R.C. Chemical processes affecting alkalis and alkaline earths during continental weathering. *Geochim. Cosmochim. Acta* **1980**, *44*, 1659–1666. [[CrossRef](#)]
39. Anderson, S.P.; Dietrich, W.E.; Brimhall, G.H. Weathering profiles, mass-balance analysis, and rates of solute loss: Linkages between weathering and erosion in a small, steep catchment. *Geol. Soc. Am. Bull.* **2002**, *114*, 1143–1158. [[CrossRef](#)]
40. Brimhall, G.H.; Dietrich, W.E. Constitutive mass balance relations between chemical composition, volume, density, porosity, and strain in metasomatic hydrochemical systems: Results on weathering and pedogenesis. *Geochim. Cosmochim. Acta* **1987**, *51*, 567–587. [[CrossRef](#)]
41. Gong, Q.; Deng, J.; Yang, L.; Zhang, J.; Wang, Q.; Zhang, G. Behaviour of major and trace elements during weathering of sericite-quartz schist. *J. Asian Earth Sci.* **2011**, *42*, 1–13. [[CrossRef](#)]
42. Rudnick, R.L.; Gao, S. Composition of the continental crust. In *Treatise on Geochemistry*; Rudnick, R.L., Ed.; Elsevier: Amsterdam, The Netherlands, 2003; Volume 3, pp. 1–64.
43. Taylor, S.R.; McLennan, S.M. *The Continental Crust: Its Composition and Evolution*; Blackwell Scientific Publication: London, UK, 1985; p. 311.
44. Gromet, P.L.; Dymek, P.F.; Haskin, L.A.; Korotev, R.L. The North American Shale Composite: Its Composition, Major and Minor Element Characteristics. *Geochim. Cosmochim. Acta* **1984**, *48*, 2469–2482. [[CrossRef](#)]
45. Ujvari, G.; Varga, A.; Balogh-Brunstad, Z. Origin, weathering and geochemical composition of loess in southwestern Hungary. *Quat. Res.* **2008**, *69*, 421–437. [[CrossRef](#)]
46. Boynton, W.V. Cosmochemistry of the rare earth elements: Meteorite studies. In *Rare Earth Element Geochemistry*; Henderson, P., Ed.; Elsevier: Amsterdam, The Netherlands, 1984; Volume 2, pp. 63–114.
47. Palme, H.; Jones, A. Solar system abundances of the element. In *Meteorite, Comets, and Planets, Treatise on Geochemistry*; Davis, A.M., Ed.; Elsevier: Amsterdam, The Netherlands, 2005; pp. 41–62.

48. Young, G.M.; Nesbitt, H.W. Processes controlling the distribution of Ti and Al in weathering profiles, siliciclastic sediments and sedimentary rocks. *J. Sediment. Res.* **1998**, *68*, 448–455. [[CrossRef](#)]
49. Gallet, S.; Jahn, B.; Van Vliet Lanoë, B.; Dia, A.; Rossello, E. Loess geochemistry and its implications for particle origin and composition of the upper continental crust. *Earth Planet. Sci. Lett.* **1998**, *156*, 157–172. [[CrossRef](#)]
50. Muhs, D.R.; Budahn, J.; Reheis, M.; Beann, J.; Skipp, G.; Fisher, E. Airborne dust transport to the eastern Pacific Ocean off southern California: Evidence from San Clemente Island. *J. Geophys. Res.* **2007**, *112*, D13203.1–D13203.17. [[CrossRef](#)]
51. Sak, P.B.; Navarre-Sitchler, A.K.; Miller, C.E.; Daniel, C.C.; Gaillardet, J.; Buss, H.L.; Lebedeva, M.I.; Brantley, S.L. Controls on rind thickness on basaltic andesite clasts weathering in Guadeloupe. *Chem. Geol.* **2010**, *276*, 129–143. [[CrossRef](#)]
52. Plank, T.; Langmuir, C.H. The chemical composition of subducting sediment and its consequences for the crust and mantle. *Chem. Geol.* **1998**, *145*, 325–394. [[CrossRef](#)]
53. Bauer, A.; Velde, B.D. *Geochemistry at the Earth's Surface: Movement of Chemical Elements*; Springer: Berlin/Heidelberg, Germany, 2014.
54. Collins, R.N.; Kinsela, A.S. The aqueous phase speciation and chemistry of cobalt in terrestrial environments. *Chemosphere* **2010**, *79*, 763–771. [[CrossRef](#)]
55. Panahi, A.; Young, G.M.; Rainbird, R.H. Behaviour of major and trace elements (including REE) during Paleoproterozoic pedogenesis and diagenetic alteration of an Archean granite near Ville Marie, Quebec, Canada. *Geochim. Cosmochim. Acta* **2000**, *64*, 2199–2220. [[CrossRef](#)]
56. Guthrie, V.A.; Kleeman, J.D. Changing uranium distributions during weathering of granite. *Chem. Geol.* **1986**, *54*, 113–126. [[CrossRef](#)]
57. Kraemer, D.; Kopf, S.; Bau, M. Oxidative mobilization of cerium and uranium and enhanced release of “immobile” high field strength elements from igneous rocks in the presence of the biogenic siderophore desferrioxamine B. *Geochim. Cosmochim. Acta* **2015**, *165*, 263–279. [[CrossRef](#)]
58. Middelburg, J.J.; Van der Weijden, C.H.; Woittiez, J.R.W. Chemical processes affecting the mobility of major, minor, and trace elements during weathering of granitic rocks. *Chem. Geol.* **1988**, *68*, 253–273. [[CrossRef](#)]
59. Zhang, L.; Ji, H.B.; Gao, J.; Li, R.; Li, J.J. Geochemical characteristics of major, trace and rare earth elements in typical carbonate weathered profiles of Guizhou Plateau. *Geochimica* **2015**, *44*, 323–336.
60. Ellis, A.S.; Johnson, T.M.; Bullen, T.D. Chromium isotopes and the fate of hexavalent chromium in the environment. *Science* **2002**, *295*, 2060–2062. [[CrossRef](#)]
61. Berger, A.; Frei, R. The fate of chromium during tropical weathering: A laterite profile from Central Madagascar. *Geoderma* **2014**, *213*, 521–532. [[CrossRef](#)]
62. Oze, C.; Bird, D.K.; Fendorf, S. Genesis of hexavalent chromium from natural sources in soil and groundwater. *Proc. Natl. Acad. Sci. USA* **2007**, *104*, 6544–6549. [[CrossRef](#)] [[PubMed](#)]
63. Braun, J.J.; Viers, J.; Dupre, B.; Polve, M.; Ndam, J.; Muller, J.P. Solid/liquid REE fractionation in the lateritic system of Goyoum, East Cameroon: The implication for the present dynamics of the soil covers of the humid tropical regions. *Geochim. Cosmochim. Acta* **1998**, *62*, 273–299. [[CrossRef](#)]
64. Boulange, B.; Colin, F. Rare earth element mobility during conversion of nepheline syenite into lateritic bauxite at Passa Quatro. Minas Gerais, Brazil. *Appl. Geochem.* **1994**, *9*, 701–711. [[CrossRef](#)]
65. Braun, J.J.; Pagel, M.; Muller, J.P.; Bilong, P.; Michard, A.; Cuillet, B. Cerium anomalies in lateritic profiles. *Geochim. Cosmochim. Acta* **1990**, *54*, 781–795. [[CrossRef](#)]
66. Aubert, D.; Stille, P.; Probst, A. REE fractionation during granite weathering and removal by waters and suspended loads: Sr and Nd isotopic evidence. *Geochim. Cosmochim. Acta* **2001**, *65*, 387–406. [[CrossRef](#)]
67. Laveuf, C.; Cornu, S. A review on the potentiality of Rare Earth Elements to trace pedogenetic processes. *Geoderma* **2009**, *154*, 1–12. [[CrossRef](#)]
68. Yusoff, Z.M.; Ngwenya, B.T.; Parsons, I. Mobility and fractionation of REEs during deep weathering of geochemically contrasting granites in a tropical setting, Malaysia. *Chem. Geol.* **2013**, *349*, 71–86. [[CrossRef](#)]
69. Krupka, K.M.; Serne, R.J. *Geochemical Factors Affecting the Behaviour of Antimony, Cobalt, Europium, Technetium, and Uranium in Vadose Sediments*; Pacific Northwest National Laboratory: Richland, WA, USA, 2002.
70. Buss, H.L.; White, A.F.; Murphy, S.F. Weathering processes in the Iacos and Mameyes Watersheds in Eastern Puerto Rico. In *Water Quality and Landscape Process of Four Watersheds in Eastern Puerto Rico*; Murphy, S.F., Stallard, R.F., Eds.; US Geological Survey: Reston, WV, USA, 2012; pp. 249–287.
71. Tan, P.; Oberhardt, N.; Dypvik, H.; Riber, L.; Ferrell, R.E. Weathering profiles and clay mineralogical developments, Bornholm, Denmark. *Mar. Petrol. Geol.* **2017**, *80*, 32–48. [[CrossRef](#)]
72. Nesbitt, H.W.; Young, G.M. Formation and diagenesis of weathering profiles. *J. Geol.* **1989**, *97*, 129–147. [[CrossRef](#)]
73. Le Blond, J.S.; Cuadras, J.; Molla, Y.B.; Berhanu, T.; Umer, M.; Baxter, P.J.; Davey, G. Weathering of the Ethiopian volcanic province: A new weathering index to characterize and compare soils. *Am. Mineral.* **2015**, *100*, 2518–2532. [[CrossRef](#)]
74. Ji, H.B.; Ouyang, Z.Y.; Wang, S.J.; Zhou, D.Q. Element geochemistry of weathering profile of dolomitite and its implications for the average chemical composition of the upper continental crust. *Sci. China Ser. D Earth Sci.* **2000**, *43*, 23–35. [[CrossRef](#)]

75. Lu, S.; Wang, S.; Chen, Y. Palaeopedogenesis of red palaeosols in Yunnan Plateau, southwestern China: Pedogenical, geochemical and mineralogical evidence and palaeoenvironmental implication. *Palaeogeogr. Palaeoclimatol. Palaeoecol.* **2015**, *420*, 35–48. [[CrossRef](#)]
76. Peucker-Ehrenbrink, B.; Miller, M.W. Quantitative bedrock geology of east and Southeast Asia (Brunei, Cambodia, eastern and southeastern China, East Timor, Indonesia, Japan, Laos, Malaysia, Myanmar, North Korea, Papua New Guinea, Philippines, far-eastern Russia, Singapore, South Korea, Taiwan, Thailand, Vietnam). *Geochem. Geophys. Geosyst.* **2004**, *5*, Q01B06. [[CrossRef](#)]
77. Derakhshan-Babaei, F.; Nosrati, K.; Tikhomrov, D.; Christl, M.; Sadough, H.; Egli, M. Relating the spatial variability of chemical weathering and erosion to geological and topographical zones. *Geomorphology* **2020**, *363*, 107235. [[CrossRef](#)]
78. Ouyang, N.; Zhang, Y.; Sheng, H.; Zhou, Q.; Huang, Y.; Yu, Z. Clay mineral composition of upland soils and its implication for pedogenesis and soil taxonomy in subtropical China. *Nature* **2021**, *11*, 9707. [[CrossRef](#)]
79. Dal’Bò, P.F.F.; Basilici, G.; Angèlica, R.S. Factors of palaeosol formation in a Late Cretaceous eolian sand sheet paleoenvironment, Marilia Formation, Southeastern Brazil. *Palaeogeogr. Palaeoclimatol. Palaeoecol.* **2010**, *292*, 349–365. [[CrossRef](#)]
80. Qiao, Y.S.; Hao, Q.Z.; Peng, S.S.; Wang, Y.; Li, J.W.; Liu, Z.X. Geochemical characteristics of the eolian deposits in southern China, and their implications for provenance and weathering intensity. *Palaeogeogr. Palaeoclimatol. Palaeoecol.* **2011**, *308*, 513–523. [[CrossRef](#)]
81. Sheldon, N.D.; Retallack, G.J.; Tanaka, S. Geochemical climofunctions from North America soils and application to palaeosols across the Eocene–Oligocene boundary. *J. Geol.* **2002**, *110*, 687–696. [[CrossRef](#)]
82. Meunier, A.; Caner, L.; Hubert, F.; El Albani, A.; Prêt, D. The weathering intensity scale (WIS): An alternative approach of the chemical index of alteration (CIA). *Am. J. Sci.* **2013**, *313*, 113–143. [[CrossRef](#)]
83. Beckford, H.O.; Chu, H.; Song, C.; Chang, C.; Ji, H. Geochemical characteristics and behaviour of elements during weathering and pedogenesis over karst area in Yunnan–Guizhou Plateau, southwestern China. *Environ. Earth Sci.* **2021**, *80*, 61. [[CrossRef](#)]
84. Condie, K.C. Chemical composition and evolution of the upper continental crust: Contrasting results from surface samples and shales. *Chem. Geol.* **1993**, *104*, 1–37. [[CrossRef](#)]
85. Kovács, J. Chemical weathering intensity of the Late Cenozoic red clay deposits in the Carpathian Basin. *Geochem. Int.* **2007**, *45*, 1056–1063. [[CrossRef](#)]
86. Kovács, J.; Fábián, S.Á.; Varga, G.; Újvári, G.; Varga, G.; Dezső, J. Plio-Pleistocene red clay deposits in the Pannonian basin: A review. *Quat. Int.* **2011**, *240*, 35–43. [[CrossRef](#)]

Disclaimer/Publisher’s Note: The statements, opinions and data contained in all publications are solely those of the individual author(s) and contributor(s) and not of MDPI and/or the editor(s). MDPI and/or the editor(s) disclaim responsibility for any injury to people or property resulting from any ideas, methods, instructions or products referred to in the content.